Critical transition between intensive and extensive active droplets

Jonathan Bauermann, Giacomo Bartolucci, Job Boekhoven, Frank Jülicher, Christoph A. Weber

Angaben zur Veröffentlichung / Publication details:

Bauermann, Jonathan, Giacomo Bartolucci, Job Boekhoven, Frank Jülicher, and Christoph A. Weber. 2025. "Critical transition between intensive and extensive active droplets." Physical Review X 15 (4): 041027. https://doi.org/10.1103/4nnd-tdky.

Critical Transition between Intensive and Extensive Active Droplets

Jonathan Bauermann,[1] Giacomo Bartolucci,[2] Job Boekhoven,[3] Frank Jülicher,[4,5,6] and Christoph A. Weber[7]

[1]Department of Physics, Harvard University, Cambridge, Massachusetts 02138, USA
[2]Department of Condensed Matter Physics, Universitat de Barcelona, 08028 Barcelona, Spain
[3]School of Natural Sciences, Department of Bioscience, Technical University of Munich, 85748 Garching, Germany
[4]Max Planck Institute for the Physics of Complex Systems, 01187 Dresden, Germany
[5]Center for Systems Biology Dresden, 01307 Dresden, Germany
[6]Cluster of Excellence Physics of Life, TU Dresden, 01062 Dresden, Germany
[7]Faculty of Mathematics, Natural Sciences, and Materials Engineering: Institute of Physics, University of Augsburg, 86159 Augsburg, Germany

(Received 6 September 2024; accepted 1 October 2025; published 12 November 2025)

Most emulsions ripen with an average droplet size increasing in time. In chemically active emulsions, coarsening can be absent, leading to a nonequilibrium steady state with monodisperse droplet sizes. By considering a minimal model for phase separation and chemical reactions maintained away from equilibrium, we show that there is a supercritical transition controlled by the conserved quantity between two classes of chemically active droplets: intensive and extensive active droplets. While intensive droplets reach a stationary size mainly controlled by the interplay between reactions and diffusion, the size of an extensive active droplet scales with the system size. For intensive droplets, growth arrests at a finite size. Thus, they can be far apart from each other and evolve independently from other droplets in an active emulsion. The growth of extensive droplets, however, arrests due to the presence of other droplets in the emulsion. In both cases, monodisperse emulsions can emerge. We show how the supercritical transition between intensive and extensive active droplets affects shape instabilities, including the division of active droplets, paving the way for the observation of successive division events in chemically active emulsions.

DOI: 10.1103/4nnd-tdky

Subject Areas: Biological Physics, Soft Matter

I. INTRODUCTION

Coarsening or ripening refers to the growth of larger domains at the expense of smaller domains that eventually shrink. For passive systems, the kinetics of coarsening stops when the system reaches equilibrium, corresponding to a single domain in a finite system. Coarsening occurs in various systems, ranging from spin systems [1], liquid emulsions [2], and crystallized precipitates [3]. The kinetics of coarsening is universal and determined by conservation laws, symmetries, and the dimension of the system [4–7].

For active systems persistently maintained away from equilibrium [8–11], the kinetics of coarsening is altered and can even be suppressed [12–17]. The paradigm is reaction-diffusion systems that give rise to nonequilibrium steady-state patterns with various spatial morphologies [18–20]. Another example is active model B+, which, in contrast to the classical model B, also accounts for contributions to the diffusive fluxes that do not arise from a free energy [21,22]. These fluxes give rise to anticoarsening with a condensed phase that stopped growing and a "bubbly" fluctuating morphology of material-poor domains [14]. Finally, suppressed ripening was also observed in liquid-liquid phase-separated systems with chemical reactions maintained away from equilibrium [12,13,23,24]. These systems are also called chemically active emulsions [11,25,26]. Chemically active emulsions are relevant to various engineered systems investigated in systems chemistry, where active droplets are models for synthetic cells or protocellular compartments [27–32]. They also provide a framework for the study of biomolecular condensates that form in living cells, organizing and regulating biochemical processes [33–36].

The formation of steady-state patterns in reaction-diffusion systems relies on the reaction flux that breaks the detailed balance of the rates. Together with diffusion, this gives rise to various reaction-diffusion length scales that are crucial but not exclusively responsible for pattern morphology. Chemical processes generically come with conservation laws for mass, and if incompressible, also for volume. It has been shown that conservation laws are key

determinants for the emerging patterns in mass-conserving reaction-diffusion systems [16,37–42].

Active emulsions also give rise to reaction-diffusion length scales. These length scales are crucial for various nonequilibrium phenomena in active emulsions, such as dividing droplets [43–45], formation of steady liquid shells [30,46,47], and the suppression of Ostwald ripening [13,32]. These interesting phenomena can be seen in minimal models [12,13,43,47]. However, these models focus on binary systems that lack conservation laws. Scenarios that take into account both conservation laws and chemical reactions with broken detailed balance are just beginning to be explored [30,32,45,48,49]. Similar to reaction-diffusion systems [41], conservation laws are expected to qualitatively alter the nature of transitions and instabilities in chemically active emulsions.

In passive, phase-separated systems with chemical reactions, the reaction-diffusion length scales do not determine the equilibrium state. In this passive case, conservation laws, i.e., so-called lever rules for quantities conserved by the chemical reactions, determine the volume of the condensed phase(s) at thermodynamic equilibrium. When the chemical reactions are maintained away from equilibrium (active emulsion), the emerging reaction-diffusion length scales compete with the conservation laws. It remains unclear to what extent the reaction-diffusion scales or the conservation law dominates the dynamics and patterning in chemically active emulsions.

In our work, we study how a single conservation law affects the pattern formation and coarsening in chemically active emulsions that were so far studied in the absence of a conserved density [12,13,43,47]. Our key finding is that when the conserved quantity itself varies between phases, a supercritical transition between intensive and extensive chemically active droplets exists; see Fig. 1 for an illustration. The control parameter for this transition is the globally conserved quantity. In the case of intensive droplets, single droplets in large systems are stationary, with droplet sizes independent of system size. For extensive droplets, the stationary droplet size increases with the system size. We show that this transition controls the collective dynamics of many droplets in active emulsions and explain how monodispersity and complex droplet morphologies can emerge in chemically active emulsions through a conservation law.

II. MINIMAL MODEL FOR AN ACTIVE EMULSION WITH A CONSERVED QUANTITY

In an incompressible binary mixture with two species that convert into each other via a chemical reaction, the total mass is conserved. However, in an incompressible binary mixture, this conserved quantity is constant in space, independent of time, and thus has no effect on the system behavior [12,13]. An incompressible mixture containing chemical reactions must therefore comprise at least three different molecule species to have a conserved quantity that can vary in space. We thus define a minimal ternary model for a chemically active emulsion with a conserved density.

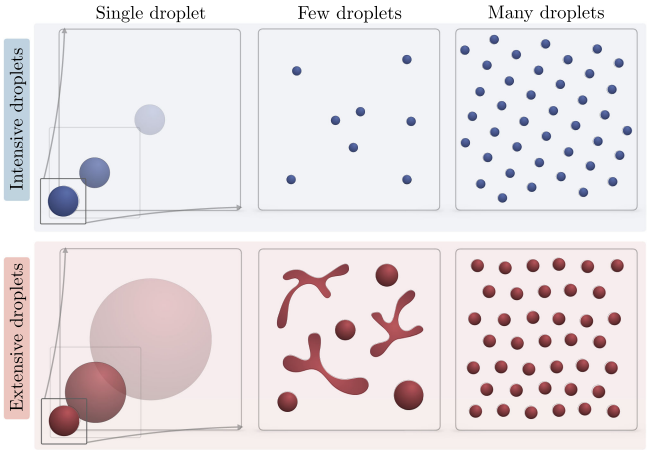

FIG. 1. Intensive and extensive active droplets and their behavior in emulsions. Chemically active emulsions undergo a transition between intensive (blue) and extensive (red) droplets. The transition depends on the value of the quantity conserved by the chemical reaction [Eq. (2)]. Intensive droplets (upper row) have finite radii and can be far apart such that they evolve independently from each other. On the contrary, extensive droplets (bottom row) grow until the presence of other droplets stops their growth.

A. Dynamics of the concentration fields

We consider an incompressible ternary mixture composed of a solvent S and the molecule species A and B, that react via the following reaction scheme:

$$A \xrightarrow{k_{BA}} B, \qquad B \xrightarrow{k_{AB}} A. \tag{1}$$

The dynamics of average concentrations $\bar{\phi}_i(t) = V^{-1}\int_V d^3x\phi_i(\boldsymbol{x},t)$ $(i = A,\ B,\ S)$ are constrained to a specific conserved line in the $\bar{\phi}_A$-$\bar{\phi}_B$ plane which can be expressed as

$$\bar{\psi} = (\bar{\phi}_A + \bar{\phi}_B)/2, \tag{2}$$

where V denotes the volume of the system and $\phi_A(\boldsymbol{x},t)$, $\phi_B(\boldsymbol{x},t)$, and $\phi_S(\boldsymbol{x},t)$ are the concentration fields that depend on position $\boldsymbol{x}$ and time t. The conserved quantity is denoted as $\bar{\psi}$.

The dynamical equations for the fields $\phi_A(\boldsymbol{x},t)$ and $\phi_B(\boldsymbol{x},t)$ of the two reacting components A and B are

$$\partial_t\phi_A = \nabla\cdot(\Gamma_{AA}\nabla\mu_A + \Gamma_{AB}\nabla\mu_B) + r, \tag{3a}$$

$$\partial_t\phi_B = \nabla\cdot(\Gamma_{BA}\nabla\mu_A + \Gamma_{BB}\nabla\mu_B) - r. \tag{3b}$$

Here, $\mu_i = \delta F/\delta\phi_i$ are the chemical potentials of $i = A, B$, descending from the Helmholtz free energy $F = \int_V d^3x(f_0 + \kappa_A(\nabla\phi_A)^2/2 + \kappa_B(\nabla\phi_B)^2/2)$, where f_0 is the free-energy density of a homogeneous system, an example of which will be given below [50]. Here, Γ denotes the mobility matrix. The first terms of Eqs. (3) are diffusive fluxes that are driven by local gradients of the chemical potentials, while the remaining term,

$$r = k_{AB}\phi_B - k_{BA}\phi_A, \tag{4}$$

is the chemical flux. For passive systems, the reaction rate coefficients k_{ij} must depend on ϕ_i via the chemical potentials, such that detailed balance of the rates is satisfied and the free energy F determines thermodynamic equilibrium [45,51]. If, however, k_{ij} are chosen independently of μ_i, the system is inherently chemically active, and when phase separated, we refer to it as chemically active emulsion [11–13,51–53].

1. Phase equilibria, molecular interactions, and the compositional angle α

Without chemical reactions, the dynamic system governed by Eqs. (3) relaxes to phase equilibrium, characterized by equal chemical potentials $\mu_i^{\mathrm{I}} = \mu_i^{\mathrm{II}}$, and equal osmotic pressures $\Pi^{\mathrm{I}} = \Pi^{\mathrm{II}}$, where $\Pi = -f + \sum_{i=A,B}\phi_i\mu_i$; see Refs. [54,55] for a general introduction. The phase diagram portrays the phase equilibria of the mixture. In Fig. 2(a), we show sketches for three different mixtures where A always phase separates from S, even when B is absent. The molecular interactions of B with A and S shape the phase diagram. In the left-hand panel of Fig. 2(a), we show a sketch of a phase diagram where B molecules are similar to S and phase separate from A, while in the central panel, we show B molecules that are neutral and do not interact differently with A or S. In the right-hand panel, B molecules are identical to A molecules and, therefore, phase separate from the solvent.

Phase equilibria are also crucial for chemically active emulsions since they locally govern the concentration change across the interface. For simplicity, we take a geometrical approach to the phase diagram. In general, the possible two-phase coexistence regions in a ternary phase diagram can be characterized by three angles describing the slopes of tie lines and binodals (see Appendix A). Here we restrict ourselves to the simple case where the slope of tie lines is described by the angle α, while tie lines remain perpendicular to the binodals [Fig. 2(b)]. Note that, within this assumption, the two binodals are always parallel to each other, such that a critical point is precluded. This scenario is captured by a Landau-Ginzburg free energy of the following form:

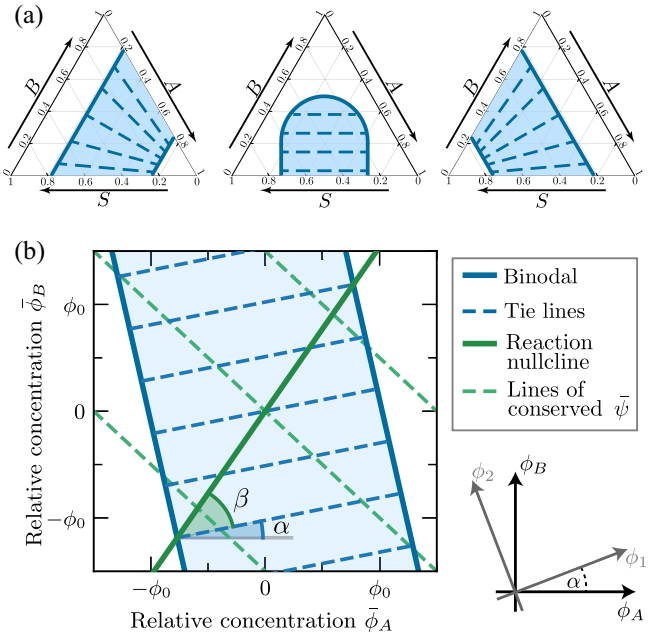

FIG. 2. Geometrical representation of phase diagram and reaction nullcline. (a) Sketches of phase diagrams of different ternary mixtures: In the white domains, the system is homogeneous, while in the blue domains, it is phase separated. Each diagram corresponds to different interactions among the molecules A, B, and S. The key qualitative properties of such diagrams can be captured by a geometrical representation. (b) Geometrical representation of a phase diagram with the binodal line (dark solid blue line), the tie lines (dashed blue line), the conserved quantities $\bar{\psi}$ (dashed green line), and the reaction nullcline (solid green line), where chemical fluxes vanish. Moreover, α is the compositional angle determining the composition of the coexisting phases, while β is the activity parameter characterizing the strength of nonequilibrium driving. Only for $\beta = 0$, there can be chemical stationary states with phase compositions that are connected by a tie line.

$$f_0(\phi_A, \phi_B; \alpha) = \frac{b_1}{2}(\phi_1 + \phi_0)^2(\phi_1 - \phi_0)^2 + \frac{b_2}{2}\phi_2^2, \tag{5a}$$

$$\begin{pmatrix}\phi_1\\ \phi_2\end{pmatrix} = \begin{pmatrix}\cos\alpha & \sin\alpha\\ -\sin\alpha & \cos\alpha\end{pmatrix}\begin{pmatrix}\phi_A\\ \phi_B\end{pmatrix}, \tag{5b}$$

where b_1 and b_2 are positive constants. Note that this parametrization gives a simple free energy that is complex enough to extract generic features when qualitatively changing the geometry of the phase diagram.

The different values of the angle α correspond to different types of interactions of the B molecules with A and solvent S. Without loss of generality, we restrict ourselves to the domain $-\pi/4 \le \alpha \le \pi/4$. Indeed, due to the symmetry of the free energy, the transformation $\alpha' = \alpha + \pi/2$ is equivalent to relabeling A to B and B to A. For $\alpha = -\pi/4$, B and A interact equally with the solvent, for $\alpha = 0$, B does not interact with A and solvent, and for

$\alpha = \pi/4$, B and S interact equally with A. As a consequence, in the case $\alpha = -\pi/4$, the two reactants A and B localize in two distinct phases; i.e., they segregate. In contrast, for $\alpha = +\pi/4$, molecules of type A and B phase separate together from the solvent S.

Following Refs. [56,57], we refer to $\alpha = -\pi/4$ as the *segregative* case and $\alpha = +\pi/4$ as *associative* case. In the literature on mixtures composed of a large number of components, these two cases are often called demixing and condensation, respectively [58]. In the literature of biomolecular condensates, the shape of the phase diagrams is often related to the underlying molecular interactions. According to Ref. [59], heterotypic interactions correspond to the segregative case and homotypic interactions to the associative case. Since the molecular interactions determine the composition of the coexisting phases, we refer to α as *compositional angle*. Varying α in the range $-\pi/4 < \alpha < \pi/4$ interpolates between the limits of the segregative and associative case.

In Fig. 2(b), we show the phase diagram associated with the free-energy density f_0 in Eq. (5). Note that the binodal lines (dark blue) separating the mixing from the demixing regimes (white and blue shaded area, respectively) are straight lines tilted by the compositional angle α from the vertical. The tie lines (dashed blue lines) are parallel to each other, perpendicular to the binodal, and thus tilted by the compositional angle α from the horizontal. Finally, we comment on the role of ϕ_0 in Eq. (5) [Fig. 2(b)]: The value ϕ_0 sets the scale of the concentration axis, since for $\cos(\alpha)\phi_A + \sin(\alpha)\phi_B$ inside the interval $[-\phi_0, \phi_0]$, the passive system can phase separate.

2. Nullclines of active chemical reactions and the activity parameter β

In a chemically active system, chemical equilibrium and phase equilibrium do not have to be reached simultaneously. Therefore, the slope of the *reaction nullcline*, which describes the steady state of the reactions defined by the condition

$$k_{AB}\phi_B = k_{BA}\phi_A, \tag{6}$$

can be at an angle that is different from the slope α of the tie line; see the solid green line in Fig. 2(b). We therefore call the angle β between tie line and reaction nullcline the activity parameter, as it controls the nonequilibrium conditions for a given phase diagram. Considering constant chemical rate coefficients k_{ij}, the activity parameter is

$$\beta = \arctan(k_{BA}/k_{AB}) - \alpha, \tag{7}$$

Indeed, only for the special case $\beta = 0$, the system is passive and can settle to thermodynamic equilibrium because in this case the coexisting concentrations at phase equilibrium are also in chemical equilibrium [Eq. (6)]. In other words, phase equilibrium with the free-energy density [Eq. (5)] implies in each phase that the ratio $\phi_B/\phi_A = \tan(\alpha)$. For $\beta = 0$, this relationship is identical to the ratio k_{BA}/k_{AB}. For $\beta \neq 0$, coexisting concentrations connected by a tie line do not lie on the reaction nullcline. Thus, no stationary state of reactions [Eq. (6)] simultaneously fulfills phase equilibrium. Instead, reaction fluxes and diffusive flux between the phases balance each other, leading to a nonequilibrium steady state. The activity parameter is restricted to the domain $0 \leq \beta < \pi/2$ because, for $\beta = \pi/2$, the reaction nullcline becomes perpendicular to the tie lines.

In summary, an active emulsion with chemical reaction Eq. (1) is characterized by the compositional angle α, the activity parameter β, and the conserved quantity $\bar{\psi}$ [Eq. (2)] and can be described by the free energy [Eq. (5)].

B. Dynamics of the conserved and nonconserved fields

To understand the role of conserved quantities in the ripening kinetics, we introduce the conserved field $\psi(\boldsymbol{x}, t)$ and the reaction extent field $\xi(\boldsymbol{x}, t)$, which are defined as

$$\psi(\boldsymbol{x}, t) = [\phi_A(\boldsymbol{x}, t) + \phi_B(\boldsymbol{x}, t)]/2, \tag{8a}$$

$$\xi(\boldsymbol{x}, t) = [\phi_A(\boldsymbol{x}, t) - \phi_B(\boldsymbol{x}, t)]/2. \tag{8b}$$

We consider a constant mobility and also write for simplicity $\Gamma_{ij} = \Gamma\delta_{ij}$, leading to the dynamic equations,

$$\partial_t\psi = \Gamma\nabla^2\mu_\psi(\psi, \xi; \alpha), \tag{9a}$$

$$\partial_t\xi = \Gamma\nabla^2\mu_\xi(\psi, \xi; \alpha) - K\xi + K\cot\left(\frac{\pi}{4} + \alpha + \beta\right)\psi, \tag{9b}$$

where we have introduced the chemical potentials $\mu_\psi = (\mu_A + \mu_B)/2$ and $\mu_\xi = (\mu_A - \mu_B)/2$ for ψ and ξ, respectively. These chemical potentials can be obtained from functional derivatives, $\mu_\psi = \delta F/\delta\psi$ and $\mu_\xi = \delta F/\delta\xi$, when expressing the free energy $f_0(\psi, \xi)$ in terms of the conserved and nonconserved fields. Furthermore, we define the overall reaction rate as

$$K = k_{AB} + k_{BA}. \tag{10}$$

The rate coefficients k_{AB} and k_{BA} can be expressed in terms of the overall rate K, the activity parameter β, and the compositional angle α; see Appendix B.

We can identify two special cases where the chemical potentials of the conserved field and of the reaction extent field decouple; i.e., coupling terms proportional to $\psi\xi$ vanish in the free energy.

(i) For $\alpha = -\pi/4$, A segregates from B, and we find $f_0(\psi, \xi) = b_2\psi^2 + 2b_1(\xi - \phi_0/\sqrt{2})^2(\xi + \phi_0/\sqrt{2})^2$.

Thus, the free-energy density contribution in the reaction extent ξ is a classical double-well potential, which leads to a Cahn-Hilliard dynamics with reactions for the reaction extent field $\xi(\boldsymbol{x},t)$ [Eq. (9b)]. The conserved field $\psi(\boldsymbol{x},t)$ undergoes simple diffusion according to Eq. (9a).

(ii) For $\alpha=\pi/4$, A and B separate together from the solvent and $f_0(\psi,\xi)=2b_1(\psi-\phi_0/\sqrt{2})^2(\psi+\phi_0/\sqrt{2})^2+b_2\xi^2$. In this case, the conserved field $\psi(\boldsymbol{x},t)$ follows a Cahn-Hilliard dynamics [Eq. (9a)], while the reaction extent field $\xi(\boldsymbol{x},t)$ undergoes simple diffusion and reactions [Eq. (9b)].

The dynamics of the conserved field ψ evolves independently from the reaction extent field in both cases (i) and (ii); however, the dynamics of the reaction extent is affected by the conserved field $\psi(\boldsymbol{x},t)$ via the reaction dynamics [Eq. (9b)]. The ripening dynamics of the two special cases (i) and (ii) corresponding to $\alpha=\pm\pi/4$ have been studied in the past.

(i) For the segregative case, $\alpha=-\pi/4$, the conserved variable ψ follows simple diffusion dynamics and settles in a homogeneous state on long timescales. Moreover, the dynamics of ξ are the dynamics of a binary mixture composed of A and B with active chemical reactions between these two components. This leads to the suppression of Ostwald ripening, i.e., a monodisperse emulsion with a stationary droplet size [12,13,23]. Once the droplet size exceeds this stationary value, droplets shrink or can undergo shape instabilities, giving rise to droplet division [43], or form stationary, active shells [30,47].

(ii) For the associative case, $\alpha=\pi/4$, the conserved variable ψ follows a classical Cahn-Hilliard dynamics. Thus, droplets rich in ψ undergo Ostwald ripening in a background of low ψ, where bigger droplets grow at the expense of smaller shrinking ones that eventually disappear. On large timescales and in a finite system, the system evolves toward a single droplet with a volume that scales with the system size V. The dynamics of the reaction extent ξ is affected by the ψ field without disturbing it. A similar decoupling of phase separation and reactions occurs in models for reacting diluted "client" particles corresponding to ξ and phase separating scaffold components corresponding to ψ [60].

In the special cases, the droplet dynamics thus exhibits very different behaviors, raising the question of how the system behavior transitions from suppressed Ostwald ripening to classical ripening dynamics in the range $-\pi/4<\alpha<\pi/4$. The key property as compared to the special cases (i) and (ii) is that the dynamics of the conserved field ψ are in general influenced by the nonconserved field ξ. In binary mixtures with active reactions [12,13], or evaporating thin films that are heated from below [61], the governing equation is a Cahn-Hilliard equation with a reaction term, sometimes called Cahn-Hilliard-Oono equation [62–64]. For the considered ternary mixtures with just one active reaction, the reaction extent ξ [Eq. (9b)] follows such a Cahn-Hilliard-Oono equation that is coupled to a Cahn-Hilliard equation for the conserved field ψ [Eq. (9a)]. This coupling arises from the molecular interactions between the components A, B, and the solvent [see Figs. 2(a) and 2(b) and related discussions].

In the next section, we will discuss the case of general α. We will show that the coupling between the conserved field and nonconserved field remains relevant in the thermodynamic limit $V\to\infty$, where V is the system volume, i.e., on length scales larger than the reaction-diffusion length scales.

III. STATIONARY SINGLE DROPLETS

To study the effects of the conserved quantity $\bar{\psi}$ on the droplet size, we first consider a single spherical droplet in a finite, spherically symmetric system of radius $R_{\mathrm{syst}}=[3V/(4\pi)]^{1/3}$. Note that the nonconserved field ξ gives rise to a reaction-diffusion length scale $\lambda=\sqrt{D/K}$, which can be obtained when linearizing near phase equilibrium. Here, $D=\Gamma\partial^2 f_0(\psi^{\pm},\xi^{\pm})^2/\partial\xi^2$, which can be calculated in our model: $D=\sqrt{\{\Gamma[b_2+4b_1\phi_0^2+(b_2-4b_1\phi_0^2)\sin(2\alpha)]\}/4}$. The reaction-diffusion length scale λ is finite and real (for $\Gamma>0$, $K>0$) for all values $-\pi/4\le\alpha\le\pi/4$ and independent of β and the conserved quantity $\bar{\psi}$. We consider a sharp interface limit, which is valid when the droplet size exceeds the width of the interface [65]. Phase equilibrium is imposed at the position of this sharp interface. This boundary condition couples the reaction-diffusion equations in each phase. These reaction-diffusion equations can be linearized near phase equilibrium at the interface; for details, see Appendix D and Ref. [45].

In the following, we discuss the stationary solutions for a single droplet, i.e., $\partial_t\psi(\boldsymbol{x},t)=0$ and $\partial_t\xi(\boldsymbol{x},t)=0$, and a stationary interface position R_{stat}. For large enough system sizes R_{syst}, we always find two solutions for R_{stat} [solid and dashed lines in Fig. 3(a)] at which the total reaction flux of every component in one phase is perfectly balanced by the diffusive flux of the same component over the interface. The lower branch (dashed line) of these two solutions is the critical nucleation radius corresponding to an unstable fixed point. The upper branch (solid line) of R_{stat} is a stable fixed point corresponding to a nonequilibrium steady state. See Appendix E, Eq. (E3), for an analytical expression of the stationary radius as a function of the activity parameter β and the compositional angle α for large system sizes.

The conserved quantity $\bar{\psi}$ [Eq. (2)] affects the nonequilibrium steady state and leads to a changed behavior of the stationary radius R_{stat} as a function of the system size R_{syst}. This changed behavior is depicted in Fig. 3(a) which shows $R_{\mathrm{stat}}(R_{\mathrm{syst}})$ for two different values of the conserved

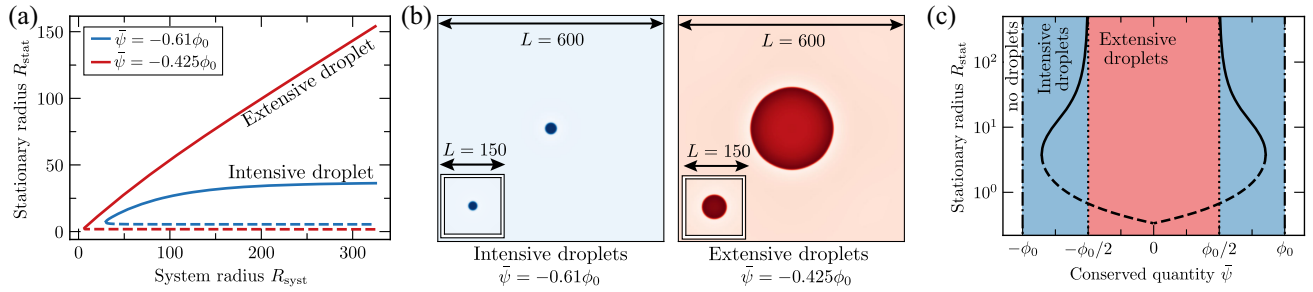

FIG. 3. Critical transition between intensive (blue) and extensive (red) active droplets. (a) There are two classes of stationary solutions, depending on the value of the conserved quantity ψ. The stationary droplet size $R_{\rm stat}$ either increases with system size $R_{\rm syst}$ (red line) or saturates for large values of $R_{\rm syst}$ (blue line). We refer to these cases as extensive (red) and intensive (blue) active droplets. Stable branches are depicted by solid lines and unstable branches are dashed. (b) Stationary concentration fields (component A) corresponding to each class [color code as in (a)] are shown for large ($L = 600$) and small systems ($L = 150$). They are obtained from numerically solving Eqs. (3). Note that the large red droplet would undergo a shape instability once the spherical droplet shape is perturbed. (c) Dependence of the stable (solid line) and unstable (dashed line) stationary radius, $R_{\rm stat}$, on the conserved quantity $\bar{\psi}$ for $\alpha = 0$ in an infinite system. The stable branch (solid line) diverges following a power law, $R_{\rm stat} \propto |\bar{\psi} - \bar{\psi}^{\pm}_{\rm crit}|^{-1}$, for $\bar{\psi} \gtrless \bar{\psi}^{\pm}_{\rm crit}$, supporting that the transition controlled by the conserved quantity is critical. Note, these stationary radii have been computed for a finite value of the surface tension, thereby leading to a gap between the onset of stationary droplets (where the stable and unstable branch converge) and the binodal (dash-dotted line). Furthermore, we show the ψ value for the critical transition between (dotted line). Because of our choice of the phase diagram, the system is symmetric around $\bar{\psi} = 0$. Note that $\bar{\psi} < 0$ corresponds to an A-rich droplet surrounded by an S-rich phase, while $\bar{\psi} > 0$ corresponds to an S-rich droplet surrounded by an A-rich phase. We color coded the regions where no droplets (white), intensive active droplet (blue), and extensive active droplet (red) exists for a system for large K, such that stationary radii get large and Laplace pressure effects can be neglected. Details on the analytical calculation of $R_{\rm stat}$ are given in Appendix E, and parameter choices for all three panels are discussed in Appendix H. All length scales in this figure are given in the terms of the interface width.

quantity $\bar{\psi} = -0.61$ (blue line) and $\bar{\psi} = -0.425$ (red line) in a system with $\alpha = 0$ and $\beta = \pi/8$. Interestingly, in the case of $\bar{\psi} = -0.61$ (blue line), the stable stationary solution converges to a finite value in the limit of large systems, i.e., $R_{\rm syst} \to \infty$, while for $\bar{\psi} = -0.425$ (red line), the solution scales linearly with the system size, for large systems. In other words, there are two different cases.

(i) *Intensive* active droplets (blue) for which the stationary droplet size $R_{\rm stat}$ quickly saturates with system size $R_{\rm syst}$ implying that $R_{\rm stat}$ is set by molecular and kinetic parameters for large system size.

(ii) *Extensive* active droplets (red) where the stationary droplet size $R_{\rm stat}$ increases linearly with system size $R_{\rm syst}$ implying that $R_{\rm stat}$ is set by $R_{\rm syst}$.

To explore these two behaviors, we numerically solved the dynamic equations with a continuous interface [Eqs. (3)] in three dimensions. Figure 3(b) shows the field $\phi_A(\boldsymbol{x})$ in four different stationary states, corresponding to the two different cases (i) and (ii) and two different system sizes ($L = 600$ and $L = 150$ in inset). We consider the same values of the conserved quantity as in Fig. 3(a). In the case of $\bar{\psi} = -0.61$ (blue), the radius of the stationary active droplet for the larger system is almost identical to that of the smaller system in the inset. In the case of $\bar{\psi} = -0.425$ (red), however, the stationary droplet radius in the larger system is much larger than in the smaller box. In Appendix C, we show additional stationary concentration fields and measure the corresponding stationary radii numerically, indicating a qualitatively different scaling behavior of $R_{\rm stat}$ between the two cases corresponding to different values of the conserved quantity $\bar{\psi}$. We conclude that the solutions of the continuous dynamic Eqs. (3) confirm the trend obtained from our single droplet study in the sharp interface limit discussed in Fig. 3(a).

The qualitative change in the scaling of the stationary radius $R_{\rm stat}$ with system size $R_{\rm syst}$ upon changing the conserved quantity $\bar{\psi}$ suggests that there is a supercritical transition between the regimes of intensive (blue) and extensive (red) active droplets. We note that with "supercritical transition" we mean a transition analogous to a supercritical bifurcation as discussed in nonlinear dynamics and pattern formation [66]. To determine the nature of this transition, we use the sharp interface model of a single droplet and consider the limit of an infinite system; for details see Appendix D. We calculate the stable (solid line) and unstable (dashed line) stationary radii $R_{\rm stat}$ as a function of the conserved quantity $\bar{\psi}$ [Fig. 3(c)]. We find that $R_{\rm stat}$ diverges at the critical values (see Appendix E for details on the derivation),

$$\bar{\psi}^{\pm}_{\rm crit} = \pm \frac{\phi_0}{2}(\cos(\alpha) + \sin(\alpha)), \tag{11}$$

where we have considered the simple case of identical diffusivities of both components in both phases, and identical reaction rates in both phases. For the general case, see Eq. (E2). In the vicinity of these critical values, the stationary droplet radius diverges with $R_{\rm stat} \propto |\bar{\psi} - \bar{\psi}^{\pm}_{\rm crit}|^{-1}$ within the domain indicated in blue in Fig. 3(c); see Appendix E. This critical behavior of $R_{\rm stat}$ is a phase transition as can be shown

by considering the ratio $R_{\mathrm{stat}}/R_{\mathrm{syst}}$ in the thermodynamic limit. It develops a kink as a function of $\bar{\psi}$ at the critical point $\bar{\psi}^{\pm}_{\mathrm{crit}}$ for large system sizes R_{syst} (Fig. 9 in Appendix F).

Furthermore, stationary active droplets can only be found within a certain range of the conserved quantity $\bar{\psi} \in [\bar{\psi}^{-}_{\mathrm{bin}}, \bar{\psi}^{+}_{\mathrm{bin}}]$ [dash-dotted black lines in Fig. 3(c)] with

$$\bar{\psi}^{\pm}_{\mathrm{bin}} = \pm \frac{\phi_0}{2} \frac{\cos(\alpha+\beta) + \sin(\alpha+\beta)}{\cos(\beta)}. \tag{12}$$

Specifically, the boundary of the region corresponding to droplets, $\bar{\psi}^{-}_{\mathrm{bin}}$ and $\bar{\psi}^{+}_{\mathrm{bin}}$, can be found locating the intersection between the reaction nullcline, the binodal curves of the phase diagram, and the contour lines of $\bar{\psi}$ [Fig. 2(b)]. Moreover, for $\bar{\psi}^{-}_{\mathrm{bin}} < \bar{\psi} < 0$, we find A-rich droplets in a solvent-rich phase, while for $0 < \bar{\psi} < \bar{\psi}^{+}_{\mathrm{bin}}$, there are solvent-rich droplets in an A-rich phase.

Through Eqs. (11) and (12), we can study how the underlying molecular interactions (parametrized by the compositional angle α) and the activity parameter β affect the existence of droplets and the supercritical transition; see Figs. 4(a) and 4(b). Neglecting the finite size effects, these results are independent of the specific values of kinetic parameters such as Γ and K, and otherwise only depend on thermodynamic parameters in the free energy [Eq. (5)]. We find that for $\beta > 0$, the active driving leads to a regime of intensive droplets for all values $-\pi/4 \leq \alpha < \pi/4$; see Fig. 4(a). Recall that in the segregative case, $\alpha = -\pi/4$ corresponds to an effective binary model of components A and B, which phase separate from each other and are converted into each other via chemical reactions; this case was studied in Ref. [13]. Only in this limiting case are droplets always intensive, and the conserved quantity does not affect the stationary radii of chemically active droplets.

For all values $-\pi/4 < \alpha < \pi/4$, there is an additional domain with extensive droplets. The transition between these two regimes occurs at a value of the conserved quantity $\bar{\psi}^{\pm}_{\mathrm{crit}}$ expressed in Eq. (11). In the associative case $\alpha = \pi/4$, $\bar{\psi}^{\pm}_{\mathrm{crit}} = \bar{\psi}^{\pm}_{\mathrm{bin}}$, i.e., no intensive droplets can be found, independently of the value of the activity parameter β. In this case, droplets behave like droplets in passive systems despite the presence of an active chemical reaction. Chemical reactions still drive diffusive fluxes of A and B between the phases. However, these fluxes do not affect the spatial distribution of the stationary conserved field $\psi(x)$. In the passive case with $\beta = 0$, we find that $\bar{\psi}_{\mathrm{bin}} = \bar{\psi}_{\mathrm{crit}}$ independent of the compositional angle α; see Fig. 4(b) leftmost panel (green domain). Indeed, passive droplets are always extensive since they behave as thermodynamic phases that scale with the system size. However, for $\beta > 0$, $\bar{\psi}^{\pm}_{\mathrm{crit}} \lesseqgtr \psi^{\pm}_{\mathrm{bin}}$. Therefore, intensive droplets of finite size exist inside a domain that increases for larger activity parameter β [see Fig. 4(b) from left to right].

The transition line [Eq. (11)] between intensive and extensive droplets is not related to a change in the nature of the instability of the homogeneous state. To show this, we performed a linear stability analysis of the homogeneous state in Appendix G. We find that there is a transition between type I and type II, following the definition in Ref. [66]. This transition, however, is unrelated to the transition from intensive to extensive chemically active droplets that was obtained analytically using a sharp interface model.

In summary, our analysis of single active droplets shows that there are two different classes of stationary states in the limit of an infinitely large system: intensive active droplets and extensive active droplets. While an intensive active droplet adopts a finite size in a large system, an extensive active droplet scales with the system size. There is a critical

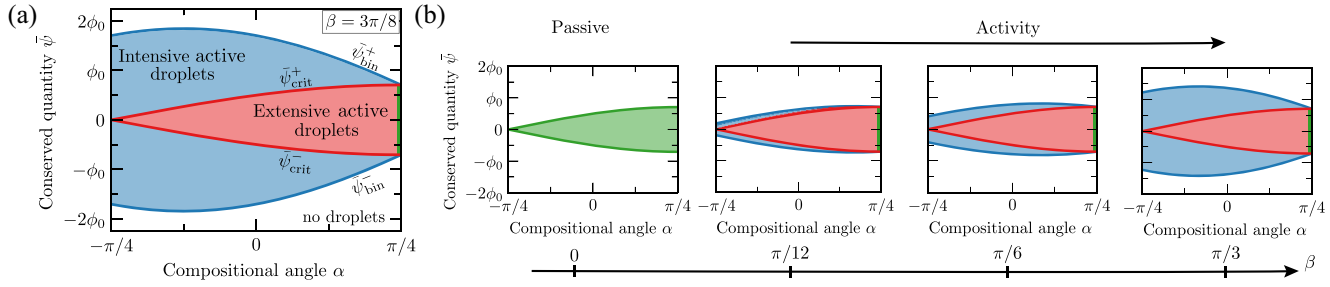

FIG. 4. State diagrams for intensive (blue) and extensive (red) active droplets. Here we show for which values of the activity parameter β [Eq. (7)], the compositional angle α [Eq. (5)], and the conserved quantity $\bar{\psi}$ [Eq. (2)] we find intensive active droplets (blue) or extensive active droplets (red). (a) For an intermediate value of the activity parameter $\beta = 3\pi/8$, we find two regimes: intensive active droplets (blue) and extensive active droplets (red). For larger compositional angles α, extensive droplets get favored. For the associative case $\alpha = \pi/4$, droplets behave like in the passive case (green line) (see Sec. VI). (b) For an active parameter of $\beta = 0$, passive droplets exist in the green domain. In the same domain, in the case $\beta > 0$, extensive droplets are found (now red domain). For $\beta > 0$, droplets behave like passive ones only in the associative case of $\alpha = \pi/4$ (green line). Furthermore, an additional regime of intensive active droplets opens up (blue domain). This regime gets wider for higher values of the activity parameter β. The boundary of extensive droplets is given by Eq. (11), and the outer boundary of intensive droplets is given by Eq. (12). For $\beta = 0$, i.e., in the passive case, both bounds collapse. Details on the analytical calculation of $\bar{\psi}^{\pm}_{\mathrm{crit}}$ are given in Appendix E, and parameter choices are listed in Appendix H.

transition between both types of nonequilibrium steady states. This transition is controlled by the interactions among the components, characterized in our model by the compositional angle α, the conserved quantity $\bar{\psi}$, and the activity parameter β. In the next section, we study emulsions composed of many active droplets and explore their behavior in the parameter regimes corresponding to intensive and extensive active droplets.

IV. INTERACTIONS OF MANY DROPLETS

In this section, we study the dynamics in active emulsions by numerically solving the dynamic equations [Eqs. (3)] for the continuous fields $\phi_A(\boldsymbol{x}, t)$ and $\phi_B(\boldsymbol{x}, t)$ with a continuous interface in three dimensions. We initialize the system in a homogeneous state at local chemical equilibrium, with the average concentration values $\bar{\phi}_A$ and $\bar{\phi}_B$ inside the binodal domain but outside of the spinodal domain. Moreover, N_{init} small spherical droplets above the critical nucleation radius are randomly positioned in the system with $\phi_A = \phi_0$ inside [Eq. (5)]. To avoid the fusion of such initially placed droplets right after initialization, we accept only random configurations with interdroplet distances above a threshold value.

We now discuss representative results corresponding to the intermediate values of the compositional angle $\alpha = 0$ and the activity parameter $\beta = \pi/8$. With this choice, Eqs. (12) and (11) imply that the bounds on the conserved quantity $\bar{\psi}$ for the existence of droplets are given by $\bar{\psi}^{\pm}_{\text{bin}} = \pm\phi_0/\sqrt{2}$ and the supercritical transition between intensive and extensive droplets is $\bar{\psi}^{\pm}_{\text{crit}} = \pm 0.5\phi_0$. The initial concentrations outside are chosen such that the total conserved quantity in the system is either $\bar{\psi} = -0.6\phi_0$ or $\bar{\psi} = -0.4\phi_0$. These two values lie, respectively, in the regime where chemically active droplets are intensive ($\bar{\psi} < \bar{\psi}^{-}_{\text{crit}}$) or extensive ($\bar{\psi}^{-}_{\text{crit}} < \bar{\psi} < \bar{\psi}^{+}_{\text{crit}}$).

The leftmost column of Fig. 5(a) (gray) depicts the initial state of the active emulsion corresponding to an initial droplet number of $N_{\text{init}} = 8$ and $N_{\text{init}} = 96$, respectively. In the remaining columns of Fig. 5(a) (blue and red), we show the stationary states of the active emulsion for these two initial conditions and the aforementioned conserved quantities $\bar{\psi} = -0.6\phi_0$ (blue) and $\bar{\psi} = -0.4\phi_0$ (red). We find that for $\bar{\psi} = -0.6\phi_0$ (intensive regime), all droplets grow to the same size; i.e., a monodisperse active emulsion emerges. During this kinetics to the stationary state, a few droplets vanish compared to the initial condition.

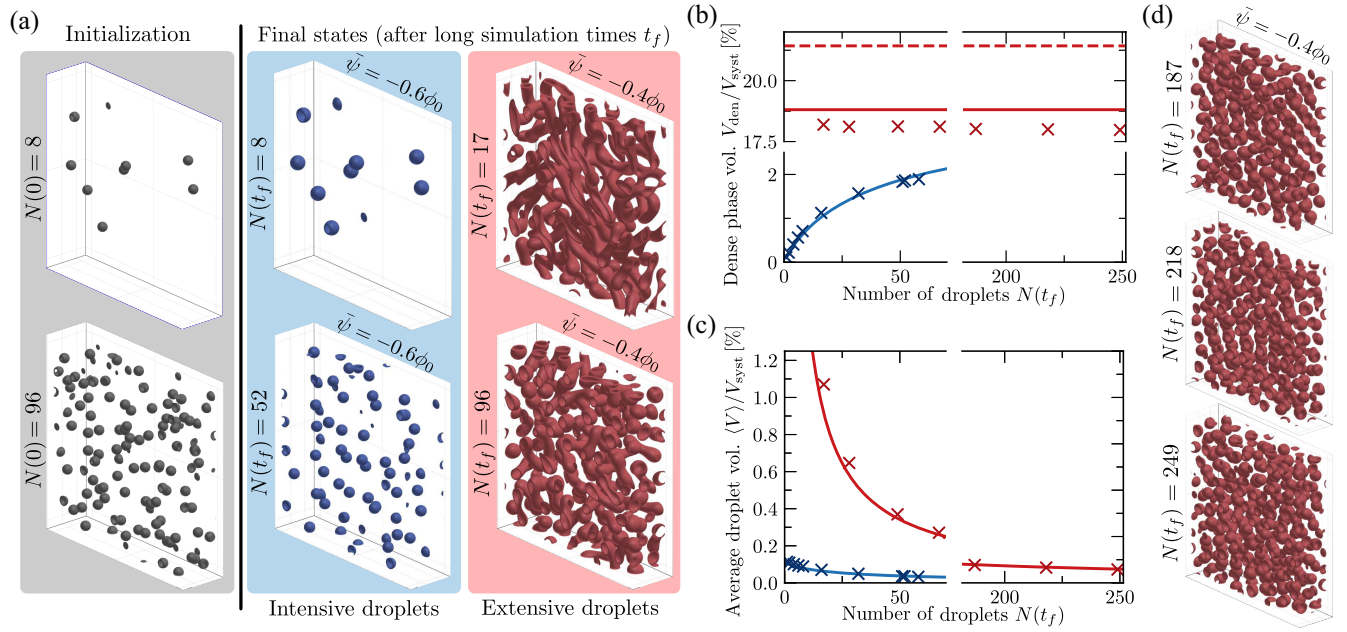

FIG. 5. Stationary states in emulsions composed of many intensive (blue) and extensive (red) active droplets. (a) Density plots of ϕ_A with $N(t)$ droplets for the initial conditions (gray) of $N(0) = 8$ and $N(0) = 96$ at time $t = 0$ and the corresponding final states after long simulation times $t_f = 5000$ [units $1/K$, Eq. (10)] for $\bar{\psi} = \phi_0$ (blue) and $\bar{\psi} = -0.4$ (red). (b) Numerically measured total volume of the dense phase $V_{\text{den}} = \langle V\rangle N$ as a function of the final droplet number $N(t_f)$ marked by red ($\bar{\psi} = -0.6\phi_0$) and blue ($\bar{\psi} = -0.4\phi_0$) cross symbols. Continuous lines show the results obtained by dividing the system volume into N equal subvolumes and carrying out the single droplets analysis. The red dashed line shows the resulting fraction of the phase volume in the limit of infinitely fast diffusion [51]. (c) Average droplet volume $\langle V\rangle = N^{-1}\sum_i^N V_i$, where V_i are individual droplet volumes. As for the upper panel, crosses correspond to numerical results, and lines correspond to the single droplet analysis. (d) Stationary concentration profiles ϕ_A for $\bar{\psi} = -0.4\phi_0$ corresponding to a final droplet number of $N(t_f) = 187$ [$N(0) = 192$], $N(t_f) = 218$ [$N(0) = 256$], and $N(t_f) = 249$ [$N(0) = 352$] from top to bottom. In all cases, $\alpha = 0, \beta = \pi/8, K = 0.0028$. After the final time $t_f = 5000$, no significant changes were detectable for all cases. Parameters used for solving the continuous model Eqs. (3) are given in Appendix H.

Interestingly, for $\bar{\psi} = -0.6\phi_0$, the stationary droplet radius changes only slightly for the two initial conditions. In the right-hand column of Fig. 5(a) (red), we show the stationary states for $\psi = -0.4\phi_0$ (above the supercritical transition, extensive regime) for the same initial conditions as above. For the initial state composed of eight droplets only (first row), droplets elongate and sometimes branch, thereby forming tubelike structures. However, some of these branched structures can separate during the dynamics such that, in the end, $N = 17$ different tubes of different lengths exist. When initializing 96 droplets (second row), some of them elongate, while others stay almost spherical, dependent on the initial distance to other droplets. However, none of them dissolve, such that we find $N = 96$ objects in the stationary state. When even more droplets are initialized, some of the initial droplets dissolve, while the rest stay spherical and try to maximize their distance toward each other; see Fig. 5(d).

Despite these complex changes in droplet morphologies, there is a common principle in the regime where single active droplets are extensive (red): Despite varying the initial conditions and different numbers of dropletlike domains in the stationary state, the total phase volume is almost constant [Fig. 5(b)]. In other words, when there are more dropletlike domains, they are smaller such that the total phase volume is approximately conserved. In contrast, in the regime where active droplets are intensive (blue), the total volume increases with the amount of initialized droplets. Most importantly, in this regime, the average droplet volume is roughly constant [Fig. 5(c)] and approximately equal to the volume of one single droplet up to finite size effects.

Monodisperisty in chemically active emulsions can be explained as follows. Intensive droplets (blue) adopt a fixed size independent of the system size. When just a few droplets are initialized in a large system, they can be far apart, and whenever they are separated by a distance much longer than the reaction-diffusion length scale in the outside phase, they hardly interact with each other. As a consequence, their dynamics becomes stationary and their average radius takes a value similar to the stationary radius R_{stat} obtained from the single droplet analysis (see Sec. III). When more droplets are initialized, such that they are closer than this reaction-diffusion length scale, they weakly interact and get stationary at smaller sizes. This leads to the slight decrease of average droplet volume for large N, seen in Fig. 5(c). In all cases, droplets reach identical radii. For extensive droplets (red), monodispersity is found only when many droplets are initialized. Indeed, when only a few droplets are initialized, they tend to grow until they feel the presence of their neighbors. The more droplets are initialized, the sooner this arrest occurs, decreasing the radii of droplets. If the number of initialized droplets is too small, droplets grow to sizes where shape instabilities can occur. Tubes form via an elongation instability, discussed in the next section, or spherical shells form via a spinodal instability at the center of large droplets [47]. Crucially, when enough droplets are present, the arrest of growth happens earlier than shape instabilities can occur. As a consequence, droplets are spherical and reach identical radii [Fig. 5(d)]. In summary, for extensive droplets in an emulsion (red), the history of the emulsion matters for the final stationary monodispersed state or the emerging shape instabilities.

To confirm the validity of these arguments relying on a single droplet analysis, we compare the phase volume and the average droplet size with the analytic results obtained from the single droplet case in the sharp interface limit. To this end, we considered N identical subsystems arranged in a hexagonal close-packed lattice that fills the total system volume V_{syst}, and calculated phase volumes and average sizes. These analytically derived results [solid lines in Figs. 5(b) and 5(c)] are in good agreement with the measured values in the numerical simulations of the active emulsions. In the case of extensive droplets [dashed lines in Figs. 5(b) and 5(c)], the total volumes of the phases are well captured by considering the limit of fast diffusion [51].

We conclude by comparing the dynamics of intensive and extensive droplets that are initially far apart in emulsions. For intensive droplets, the droplet radius is fixed by a balance between reaction and diffusion and all droplets stop growing independently of each other. Here, the conserved quantity reaches a constant value between droplets and no material is exchanged between them. In contrast, extensive droplets that are far apart from each other continue to grow. For this growth to occur, conserved material must be transported toward the droplets. This transport can result only from gradients of the conserved field far apart from the droplets. Thus, even when droplets are much farther apart than any reaction-diffusion length scale, they are still coupled via the conserved field. Eventually, when sufficient conserved material is stored within the droplets, the concentration far from the droplets is low enough such that growth stops. Recently, this self-organized arrest of ripening was studied by coupling the dynamics of single droplets via a global conservation law [67], in a manner analogous to the classic Lifshitz-Slyozov-Wagner theory, which describes the evolution of droplet size distributions during ripening in emulsions [4,5].

V. SHAPE INSTABILITIES AND DROPLET DIVISION

In the previous section, we have seen that for extensive active droplets in an emulsion an elongation instability can occur. This instability is reminiscent of the Mullins-Sekerka instability that occurs in the diffusive growth of a single droplet without reactions in a large system. It requires a (weak) deformation of a droplet's spherical shape and relies on the material depositing at interfacial domains of larger mean curvature. As a result, these

domains grow faster, further deforming the droplet shape. Deformations are counteracted by surface tension, which tends to flatten the mean curvatures of the interface. However, this effect weakens as the droplet becomes larger. Thus, there is a critical radius above which droplets constantly grow and deform (Mullins-Sekerka instability).

A similar instability can occur for both extensive and intensive active droplets. Indeed, in a binary mixture where droplets are always intensive, such instability was shown to lead to droplet division [43]. Here, we show that droplet dynamics after elongation vastly differ between intensive and extensive active droplets. In the upper row of Fig. 6 (blue), we show snapshots of the dynamics of two intensive droplets ($\bar{\psi} = -0.6\phi_0$) and compare it to the dynamics of two extensive droplets ($\bar{\psi} = -0.4\phi_0$) in the lower row (red). For both cases, we choose identical kinetic parameters. However, we have chosen the overall reaction rate K [Eq. (10)] such that the stationary droplet radius in the intensive regime exceeds the critical radius for onset of the elongation instability. In both cases, the two droplets are initially separated by a distance smaller than the reaction-diffusion length in the outside phase. Thus, the presence of the neighboring droplets leads to asymmetries that induce initial deformations, which get amplified by the elongation instability. However, the division predominantly happens for intensive droplets; see Fig. 6 (upper row). Extensive droplets elongate (Fig. 6, lower row) and form tubes, as seen before. This difference can be explained by focusing on the neck region. For intensive droplets, there is almost no growth in this region, such that a Plateau-Rayleigh instability can lead to a pinch-off. However, extensive droplets constantly grow, including in the neck region, thereby inhibiting the Plateau-Rayleigh instability.

Interestingly, with such cycles of growth and division of intensive droplets, the total phase volume can trivially grow just by increasing the number of droplets. As a result, these shape instabilities allow intensive droplets to fill the space.

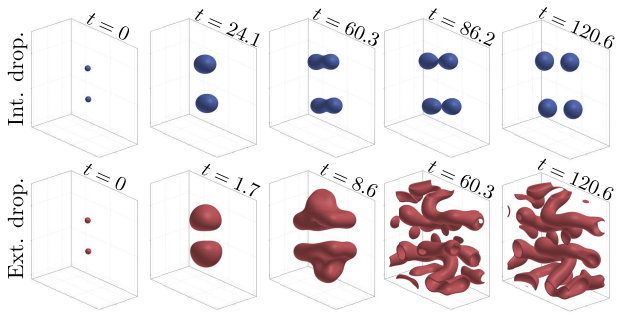

FIG. 6. Time evolution of shape unstable intensive (blue) and extensive (red) active droplets. Snapshots of concentration profile ϕ_A for a conserved quantity $\bar{\psi} = -0.6\phi_0$ (blue, upper row) and $\bar{\psi} = -0.4\phi_0$ (red, lower row). While intensive droplets divide, extensive droplets undergo a Mullins-Sekerka instability and form complex tubelike morphologies. For parameter choices, see Appendix H.

Thus, macroscopic phase volumes are reached, even in infinite systems, similar to the regime of extensive droplets.

VI. MOLECULAR INTERACTIONS AFFECT THE ARREST OF RIPENING

In Sec. IV, we have shown that extensive droplets grow until the interaction with neighboring droplets arrests their growth. However, in Sec. II B, we discussed that in the associative case ($\alpha = \pi/4$), where A and B have identical interactions with the solvent, the conserved field decouples from the active driving, leading to passive phase-separating dynamics. In this section, we study how the emulsion dynamics is affected as molecular interactions approach the limit of the associative case ($\alpha \to \pi/4$). We find that extensive droplets can initially ripen like in the passive case until the effects of the active driving manifest and ripening arrests.

In Fig. 7(a), we show snapshots of the dynamics of concentration field ϕ_A for four different values of the compositional angle α; see Supplemental Material for videos on the ripening dynamics [68]. All numerical calculations are conducted with the same kinetic parameters, an activity parameter $\beta = \pi/4$, and a conserved quantity of $\bar{\psi} = -0.35\phi_0$. For these settings, all systems are populated by extensive droplets. We Initialize at $t = 0$ (not shown in the figure) homogeneous concentration profiles at the chemical steady state with small fluctuations (around 0.1% of $\bar{\psi}$). For the values of the compositional angle α considered, the system is within the spinodal regime of a nonreacting phase-separating mixture. For triggering the nucleation of many droplets, shown in the first row in Fig. 7, we did not allow for chemical reactions in the early times of the spinodal instability ($t \approx 2$). Insights on the change of the nucleation dynamics in chemically active systems can be found here [69,70]. While the nucleation process is similar for all the compositional angles α considered here, the longtime ripening dynamics depend strongly on α. For $\alpha = 0.19\pi$ [first row in Fig. 7(a), in red], some of the initial droplets dissolve, but the interaction between droplets causes the ripening to arrest. As the interaction of A and B with the solvent gets more similar, i.e., $\alpha \to \pi/4$ (associative case), this arrest of ripening occurs at a later stage of the dynamics. Prior to the arrest of ripening, smaller droplets dissolve while larger ones grow. Thus, as the arrest occurs and the emulsion becomes monodisperse, stationary droplet radii are larger as $\alpha \to \pi/4$ (associative case); see second ($\alpha = 0.23\pi$) and third ($\alpha = 0.24\pi$) row of Fig. 7(a), in red. Only in the associative case $\alpha = \pi/4$, the arrest is absent and chemically active droplets ripen as passive emulsions [last row in Fig. 7(a), in green]. This means that the classical power laws of Ostwald ripening hold in the associative case ($\alpha = \pi/4$) with $\langle R \rangle \propto t^{1/3}$ and $N \propto t^{-2/3}$ [7], while for decreasing values of $\alpha < \pi/4$, the transition to such

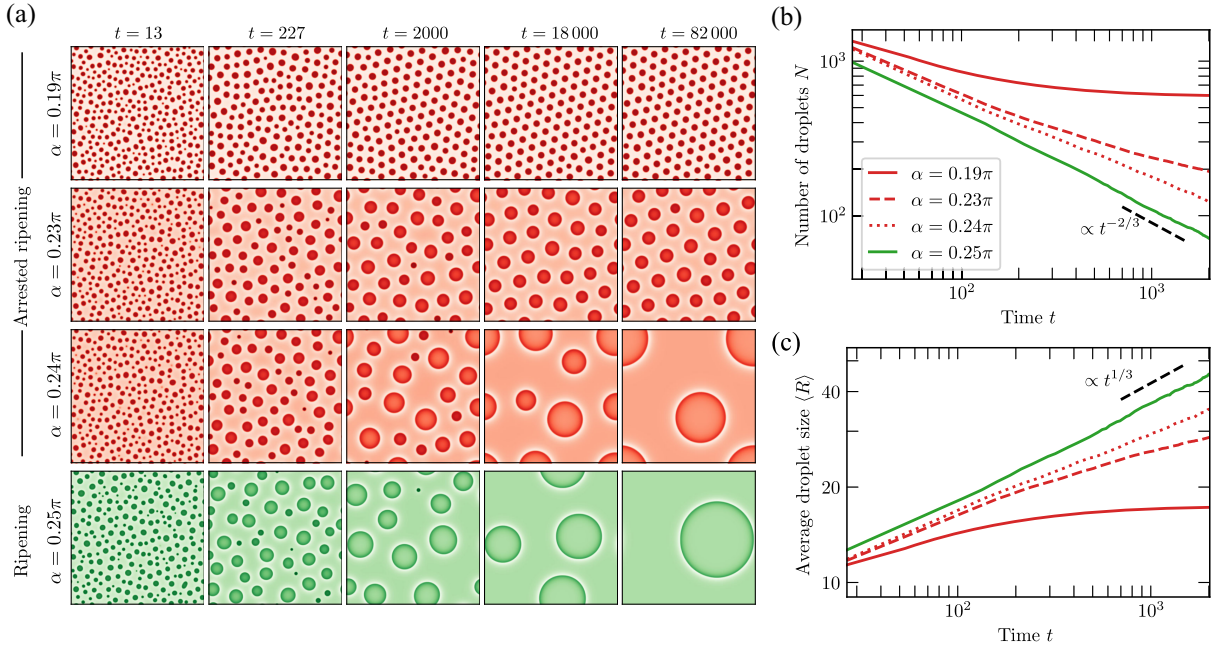

FIG. 7. Arrested ripening of extensive active droplets (red). (a) Snapshots of concentration field ϕ_A evolving in time, for an activity parameter $\beta = \pi/4$ and four different values of the compositional angle ($\alpha = 0.19\pi, 0.23\pi, 0.24\pi, 0.25\pi$, from top to bottom), each corresponding to different molecular interactions. All simulations are initialized using the concentration fields shortly after the spinodal instability of the homogeneous chemical steady state with $\bar{\psi} = -0.35\phi_0$ has occurred. (b),(c) Droplet number N and average droplet radius $\langle R \rangle$ as a function of time, for the same values of α. Passive scaling laws are indicated with dashed black lines. Parameters are given in Appendix H.

classical ripening laws happens at later stages of the dynamics [see Figs. 7(b) and 7(c)].

VII. DISCUSSION

We have introduced and studied a model of a minimal ternary mixture of the components A, B, and solvent that can phase separate while A and B convert into each other. This conversion is maintained away from chemical equilibrium by choosing reaction fluxes independent of the chemical potentials. This choice prevents the system from simultaneously reaching chemical and phase equilibrium and allows it to adopt a nonequilibrium steady state. The model is minimal because it exhibits a nontrivial conserved quantity of the reaction with an associated conserved field that is generally position dependent, also in the nonequilibrium steady state. Within this minimal model for active chemical reactions in phase-separating mixtures, we found a supercritical transition describing the transition between a single droplet that scales with system size (extensive active droplet), like in passive systems, and droplets with a characteristic size (intensive active droplet).

The transition found in the single droplet analysis has crucial consequences for the behavior of emulsions composed of many droplets. For a value of the conserved quantity in the regime of an intensive droplet, a monodisperse emulsion forms where the average size is approximately given by the stationary size of a single droplet. The reason for this approximate agreement is that droplets can be far apart from each other, such that the dynamics of single droplets decouples from other droplets in the emulsion. In contrast, extensive droplets in an emulsion constantly grow until they come close enough to interact strongly with each other. Once they interact, there can be initial ripening, but growth arrests. The morphology of the resulting structures depends crucially on initial conditions, i.e., the history of the emulsion. In other words, few droplets deform via shape instabilities, while many droplets remain spherical and monodisperse. However, the total phase volume is independent of the number and sizes of droplets and scales with the system volume similar to passive thermodynamic phases.

Our findings highlight the importance of several components in chemically active systems. For example, accounting for a solvent component fundamentally alters the dynamics of chemically active droplets, reflected in the appearance of the critical transition when varying the conserved quantity. We propose that understanding the effects of the conserved quantities(s) in reacting system away from equilibrium is crucial to correctly interpret emulsion dynamics in biological and chemical systems [32–36]. Specifically, our theory can unravel the conserved quantity's effects in synthetic chemical systems, such as droplet size control in multicomponent mixtures leading to chemically active coacervates [32]. According to our theory, droplet division is more likely to occur in the regime

$\alpha \simeq -\pi/4$, corresponding to intensive active droplets and the case where A segregates from B (segregative case). We propose studying a single active droplet in a reaction container for different container sizes [71] and test whether or not the active droplet scales with the container size [intensive active droplets see Fig. 3(a)]. In the regime of intensive active droplets, division is more likely to be obtained. This procedure could be used to test synthesized actively reacting components for their division propensity and may thus pave the way to observe successive division events in larger, mass-supplied containers containing many active droplets.

Future avenues are related to integrating our findings into the large canon of pattern-forming systems and establishing a link to physically very different systems, such as hydrodynamic instabilities governed by mathematically similar dynamic equations [61]. In particular, in our work, the dynamics of the conserved field is coupled via molecular interactions, which lead to phase separation, to the nonconserved field. Only the latter is actively maintained away from equilibrium. However, even in the thermodynamic limit of large length scales and timescales, this local driving of the nonconserved field changes the ripening dynamics of the conserved field. Understanding the large-scale consequences in systems that are locally maintained away from equilibrium is a key challenge in mass-conserving reaction-diffusion systems [16,37–42], and other active matter systems, like active model B+ [17,21,72] or nonreciprocal Cahn-Hilliard models [73–77]. Future studies will address the differences and similarities of such systems to chemically active emulsions.

APPENDIX A: GEOMETRIC PARAMETRIZATION OF A TERNARY PHASE DIAGRAM

The local properties of two-phase coexistence in a ternary phase diagram can be characterized by specifying the orientation angles of tie lines and binodals at a reference point. Given the four equilibrium concentrations $\hat{\phi}^{\pm}_{A/B}$, obtained via the common tangent construction [11], the slope of the tie line is defined by the angle $\alpha = \arctan[(\hat{\phi}^{+}_{B} - \hat{\phi}^{-}_{B})/(\hat{\phi}^{+}_{A} - \hat{\phi}^{-}_{A})]$. Furthermore, we define the angles characterizing the binodals at one reference point as $\sigma^{\pm} = \arctan(\delta\phi^{\pm}_{B}/\delta\phi^{\pm}_{A})$, where $\delta\phi^{\pm}_{i}$ are the perturbations of the equilibrium concentration along the binodals. Perturbing the equations corresponding to phase equilibrium [11] to linear order in $\delta\phi^{\pm}_{i}$ leads to the conditions

$$\tan(\sigma^{\pm}) = -\frac{(\hat{\phi}^{-}_{A} - \hat{\phi}^{+}_{A})\frac{\partial\mu_A(\hat{\phi}^{\pm}_{A},\hat{\phi}^{\pm}_{B})}{\partial\phi_B} + (\hat{\phi}^{-}_{B} - \hat{\phi}^{+}_{B})\frac{\partial\mu_B(\hat{\phi}^{\pm}_{A},\hat{\phi}^{\pm}_{B})}{\partial\phi_B}}{(\hat{\phi}^{-}_{A} - \hat{\phi}^{+}_{A})\frac{\partial\mu_A(\hat{\phi}^{\pm}_{1},\hat{\phi}^{\pm}_{B})}{\partial\phi_A} + (\hat{\phi}^{-}_{B} - \hat{\phi}^{+}_{B})\frac{\partial\mu_B(\hat{\phi}^{\pm}_{A},\hat{\phi}^{\pm}_{B})}{\partial\phi_A}}. \tag{A1}$$

The simple choice of the free energy f_0 discussed in the main text corresponds to $\sigma^{+} = \sigma^{-} = \pi/2 + \alpha$, where the binodals are parallel to each other and perpendicular to the tie lines.

APPENDIX B: CHEMICAL REACTION RATES

In the main text, we will use the overall rate $K = k_{AB} + k_{BA}$ and the activity parameter β as parameters for the chemical reactions. These parameters are related to the forward rate k_{BA} and backward rate k_{AB}, appearing in Eq. (3) via the following relationships: $k_{BA} = K\sin(\alpha+\beta)/[\cos(\alpha+\beta) + \sin(\alpha+\beta)]$ and $k_{AB} = K\cos(\alpha+\beta)/[\cos(\alpha+\beta) + \sin(\alpha+\beta)]$, where α is the compositional angle. Using this parametrization, the contour lines of $\bar{\psi}$, where the conserved quantity is constant, have a fixed slope of -1 that is independent of the compositional angle α. However, note that the slope of the chemical steady state changes when varying α. Moreover, changes in α do not affect the activity in the system, in the sense that they do not alter the angle between the reaction nullcline and the tie lines. Thus, with this parametrization, we can vary the compositional angle α for studying how different interactions affect active droplets while keeping the activity parameter β fixed. The rate K sets only a timescale.

APPENDIX C: NUMERICAL STUDY OF EXTENSIVE AND INTENSIVE SCALING

In Fig. 3(a), we illustrate how the stationary droplet sizes scale differently for extensive and intensive droplets in spherically symmetric, three-dimensional systems, as the

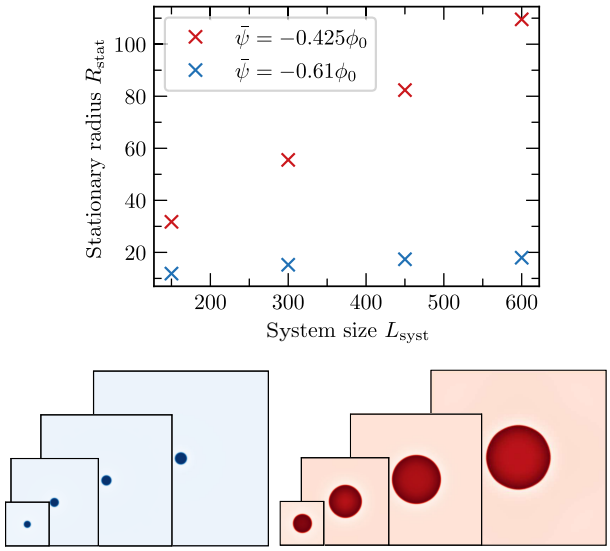

FIG. 8. Stationary radii of extensive and intensive droplets in two-dimensional systems of different size (top) and the corresponding concentration fields (component A) (bottom). Same parameter as in Fig. 3(b).

system size R_{syst} is varied. These stationary droplet radii were determined by analytically solving for the stationary state in the sharp-interface limit.

Figure 3(b) presents the stationary concentration fields for two different system sizes in two dimensions, for both extensive and intensive droplets. These results were obtained numerically. In Fig. 8, we show these concentration fields, corresponding to a small and large system sizes, together with examples of intermediate system sizes (bottom row). We then fit circles to these profiles in order to extract the stationary droplet radii, and plot these radii as a function of the system size L_{syst} of the two-dimensional square system (top row).

Despite the difference in dimensionality, two dimensional vs three dimensional, and the different geometry, spherical symmetric vs square geometry, does not allow a direct comparison between the analytical results in Fig. 3(a) and the numerical results in Fig. 8, both methods show the same qualitative scaling between extensive and intensive droplets.

Note that in the numerical studies, we initialized spherical droplets close to the stationary radius. This choice is essential to prevent shape instabilities and the formation of spherical shells [30,47].

APPENDIX D: SHARP-INTERFACE LIMIT

Similar to the droplet dynamics of passive phases (see Ref. [65] for example), we can study the dynamics of a single active droplet in the limit of a sharp interface. This approach for general multicomponent mixtures is discussed in detail in Ref. [45]. In this appendix, we derive the stationary state conditions of a chemically active droplet in the sharp-interface limit for a ternary mixture described by the free energy given in Eqs. (5). With this choice of free energy, analytical results for the stationary radius and the critical value for the transition between intensive and extensive active droplets can be determined.

For a single droplet with radial symmetry sitting at the origin (r being the radial coordinate), we split the field into two domains (inside and outside, abbreviated in/out in the following) and couple these domains via boundary conditions at an interface at position $r = R$. Furthermore, we linearize the dynamics of the fields ϕ_A and ϕ_B in Eqs. (3) around the corresponding ϕ values at the interface. In this approximation, the stationary state of a chemically active droplet in our ternary mixture is determined by the ϕ values of A/B on both sides of the interface, named Φ_A^{in}, Φ_A^{out}, Φ_B^{in}, and Φ_B^{out}, and the interface position R. In the following, we explain how these five values are determined.

Locally, at the interface, we assume an equilibrium of phase separation, i.e., identical chemical potentials and osmotic pressure across the interface. Furthermore, global conservation laws and vanishing flux differences across the interface fix a unique phase equilibrium locally at the interface and, therefore, a unique nonequilibrium steady state of the droplet; see Ref. [45].

For our simple free-energy model Eq. (5), we can obtain the four values of $\Phi_i^{\mathrm{in/out}}$ generally as a function of R and α. The determination of the stationary position of the interface R_{stat} additionally needs flux relations (see below). Assuming local phase equilibrium at the interface constrains its concentrations to the two straight binodal lines shown in Fig. 2(b) for an infinitely large system. Laplace pressure effects of an interface with surface tension γ of finite-sized droplets are corrected up to linear order via the so-called Gibbs-Thomsom coefficients c [13]. We parametrize this phase equilibrium by the intersection of its tie line with the ϕ_2 axis in its ϕ_1 and ϕ_2 representation [as defined in Eq. (5)]. This intersection we call ϕ_2^{inter}, and write

$$\begin{pmatrix} \Phi_A^{\mathrm{in/out}} \\ \Phi_B^{\mathrm{in/out}} \end{pmatrix} = \begin{pmatrix} \cos\alpha & -\sin\alpha \\ \sin\alpha & \cos\alpha \end{pmatrix} \begin{pmatrix} \pm\phi_0 + \gamma c H \\ \phi_2^{\mathrm{inter}} \end{pmatrix}, \tag{D1}$$

where we assumed that the conserved quantity is enriched inside and diluted outside. For such a spherical symmetric droplet, the mean curvature H is given by $H = 2/R$. If the dilute phase builds up the spherical droplet, the two labels in/out in Eq. (D1) have to be swapped and $H = -2/R$. Finally, we have to determine the intersection ϕ_2^{inter} via a global conservation law of the conserved quantity. Therefore, we note that while ϕ_A and ϕ_B have gradients in space, the conserved quantity is constant in space but jumps at the interface. Thus, for a finite radial-symmetric system (system size R_{syst}) with an average amount of the conserved quantity $\bar{\psi}$, we know

$$\frac{1}{2}(\Phi_A^{\mathrm{in}} + \Phi_B^{\mathrm{in}})R^3 + \frac{1}{2}(\Phi_A^{\mathrm{out}} + \Phi_B^{\mathrm{out}})(R_{\mathrm{syst}}^3 - R^3) = \bar{\psi} R_{\mathrm{syst}}^3. \tag{D2}$$

Using Eq. (D1), we find

$$\phi_2^{\mathrm{inter}} = \frac{2RR_{\mathrm{syst}}^3\bar{\psi} + [2\phi_0 R^4 - (2c\gamma + \phi_0 R)R_{\mathrm{syst}}^3][\cos(\alpha) + \sin(\alpha)]}{RR_{\mathrm{syst}}^3[\cos(\alpha) - \sin(\alpha)]}. \tag{D3}$$

In an infinite system, however, the finite-sized droplet does not contribute to the average. Thus, the outside concentrations must fulfill

$$\bar{\psi} = \frac{1}{2}(\Phi_A^{\mathrm{out}} + \Phi_B^{\mathrm{out}}), \tag{D4}$$

and therefore, again by using Eq. (D1), we find

$$\phi_2^{\mathrm{inter}} = \frac{2R\bar{\psi} - (2c\gamma + \phi_0 R)[\cos(\alpha) + \sin(\alpha)]}{R[\cos(\alpha) - \sin(\alpha)]}. \tag{D5}$$

We note by passing that it is only possible to derive the interface concentrations independently of the diffusivities and kinetic reaction rates due to our very symmetric form of the free-energy density. Thus, these kinetic coefficients have to be taken into account only for the derivation of the stationary radius. In general, all five values have to be determined in parallel, a step that typically requires numerical solving schemes; see Ref. [45].

An interface can only be stationary when the diffusive fluxes $j_i^{\mathrm{in/out}}$ are balanced across the interface, i.e., $j_A^{\mathrm{in}}(R) = j_A^{\mathrm{out}}(R)$, and $j_B^{\mathrm{in}}(R) = j_B^{\mathrm{out}}(R)$. These diffusive fluxes in the stationary state arise from the stationary concentration profiles $\phi_i^{\mathrm{in/out}}(r)$ via $j_i^{\mathrm{in/out}} = -D_i^{\mathrm{in/out}}\partial_r\phi_i^{\mathrm{in/out}}(r)$, where $D_i^{\mathrm{in/out}}$ is the diffusion coefficient of component i in the corresponding domain obtained by linearizing. By construction, it is guaranteed that $j_A^{\mathrm{out}} = -j_B^{\mathrm{out}}$ and $j_A^{\mathrm{in}} = -j_B^{\mathrm{in}}$, such that once one of the flux balances is fulfilled, the second follows trivially. Therefore, we derive only $j_A^{\mathrm{in/out}}$ in the following.

After linearizing, we can determine these fluxes through the analytical stationary ϕ_A profiles in the two domains (solving the corresponding inhomogeneous Laplace equation in radial symmetry). From here, we can derive the total flux profiles, including the fluxes at the interface. We find

$$j_A^{\mathrm{in}}(R) = (\Phi_B^{\mathrm{in}}(R)k_{AB}^{\mathrm{in}} - \Phi_A^{\mathrm{in}}(R)k_{BA}^{\mathrm{in}}) \times \left(\frac{\coth(\lambda^{\mathrm{in}}R)}{\lambda^{\mathrm{in}}} - \frac{1}{(\lambda^{\mathrm{in}})^2R}\right), \tag{D6}$$

where the rates k_{ij}^{in} are the linrearized reaction rates from Eqs. (3) and $\lambda^{\mathrm{in}} = \sqrt{(D_A^{\mathrm{in}}k_{AB}^{\mathrm{in}} + D_B^{\mathrm{in}}k_{BA}^{\mathrm{in}})/(D_A^{\mathrm{in}}D_B^{\mathrm{in}})}$. Note that we use the dependency of the interface concentration $\Phi_i^{\mathrm{in}}(R)$ on the position of the interface R derived above, see Eq. (D5). However, in the outside domain ($r > R$), the solutions read

$$j_A(R)^{\mathrm{out}}(R) = (\Phi_B^{\mathrm{out}}(R)k_{AB}^{\mathrm{out}} - \Phi_A^{\mathrm{out}}(R)k_{BA}^{\mathrm{out}}) \frac{\lambda^{\mathrm{out}}(R - R_{\mathrm{syst}})\cosh[\lambda^{\mathrm{out}}(R - R_{\mathrm{syst}})] + [(\lambda^{\mathrm{out}})^2RR_{\mathrm{syst}} - 1]\sinh[\lambda^{\mathrm{out}}(R - R_{\mathrm{syst}})]}{(\lambda^{\mathrm{out}})^2R\{\lambda^{\mathrm{out}}R_{\mathrm{syst}}\cosh[\lambda^{\mathrm{out}}(R - R_{\mathrm{syst}})] + \sinh[\lambda^{\mathrm{out}}(R - R_{\mathrm{syst}})]\}}, \tag{D7}$$

for a finite radial symmetric system with a no-flux boundary condition at the system size R_{syst}, or

$$j_A(R)^{\mathrm{out}}(R) = -(\Phi_B^{\mathrm{out}}(R)k_{AB}^{\mathrm{out}} - \Phi_A^{\mathrm{out}}(R)k_{BA}^{\mathrm{out}}) \times \frac{k_{BA}^{\mathrm{out}} + \frac{D_A^{\mathrm{out}}}{D_B^{\mathrm{out}}}k_{AB}^{\mathrm{out}} + (k_{AB}^{\mathrm{out}} + k_{BA}^{\mathrm{out}})\lambda^{\mathrm{out}}R}{(k_{AB}^{\mathrm{out}} + k_{BA}^{\mathrm{out}})(\lambda^{\mathrm{out}})^2R}, \tag{D8}$$

for infinite large systems, where again k_{ij}^{out} are the linearized reaction rates from Eqs. (3) and $\lambda^{\mathrm{out}} = \sqrt{(D_A^{\mathrm{out}}k_{AB}^{\mathrm{out}} + D_B^{\mathrm{out}}k_{BA}^{\mathrm{out}})/(D_A^{\mathrm{out}}D_B^{\mathrm{out}})}$. The stationary droplet radii can now be found by using the interface concentrations stated in Eq. (D1) and Eqs. (D3) or (D5), and numerically searching for the positions R at which Eq. (D6) equals Eq. (D7) or (D8), depending on the system size.

APPENDIX E: CRITICAL VALUE ψ_{crit} AND THE SCALING OF THE STATIONARY RADIUS IN ITS VICINITY

In Appendix D, we explained how the stationary droplet radii can be obtained in the sharp-interface limit. Here, we argue first how we can obtain the value of the conserved quantity at the transition in an infinite system and, second, show how the stationary radius scales in the vicinity of this transition.

To find the critical value of the conserved quantity, we balance the fluxes across the interface for an infinitely large droplet,

$$\lim_{R\to\infty} j_A^{\mathrm{in}}(R) = \lim_{R\to\infty} j_A^{\mathrm{out}}(R), \tag{E1}$$

from Eqs. (D6) and (D8). When Eqs. (D1) and (D5) are applied in these expressions, a dependency on the average conserved quantity $\bar{\psi}$ follows. We find that there is only one value of this conserved quantity for which Eq. (E1) is true. This value reads

$$\bar{\psi}_{\mathrm{crit}} = -\frac{\phi_0}{2}\frac{(D_A^{\mathrm{in}}k_{AB}^{\mathrm{in}} + D_B^{\mathrm{in}}k_{BA}^{\mathrm{in}})(k_{AB}^{\mathrm{out}} + k_{BA}^{\mathrm{out}}) + D_A^{\mathrm{in}}D_B^{\mathrm{in}}\lambda^{\mathrm{in}}\lambda^{\mathrm{out}}[(k_{AB}^{\mathrm{in}} - k_{BA}^{\mathrm{in}})\cos(2\alpha) + (k_{AB}^{\mathrm{in}} + k_{BA}^{\mathrm{in}})\sin(2\alpha)]}{\sin(\alpha)((D_A^{\mathrm{in}}k_{AB}^{\mathrm{in}} + D_B^{\mathrm{in}}k_{BA}^{\mathrm{in}})[k_{BA}^{\mathrm{out}} + k_{AB}^{\mathrm{out}}\cot(\alpha)] + D_A^{\mathrm{in}}D_B^{\mathrm{in}}\lambda^{\mathrm{in}}\lambda^{\mathrm{out}}[k_{BA}^{\mathrm{in}} + k_{AB}^{\mathrm{in}}\cot(\alpha)])}. \tag{E2}$$

When we apply our parametrization of the reaction rates, i.e., $k_{AB}^{\mathrm{in/out}} = K^{\mathrm{in/out}}\cos(\alpha+\beta)/[\cos(\alpha+\beta)+\sin(\alpha+\beta)]$ and $k_{BA}^{\mathrm{in/out}} = K^{\mathrm{in/out}}\sin(\alpha+\beta)/[\cos(\alpha+\beta)+\sin(\alpha+\beta)]$, see Appendix B, we find $\bar{\psi}_{\mathrm{crit}}$ as a function of the kinetic rates $K^{\mathrm{in/out}}$, diffusivities $D_i^{\mathrm{in/out}}$, and the angles α and β. With the assumptions $D_A^{\mathrm{in}} = D_A^{\mathrm{out}}$, $D_B^{\mathrm{in}} = D_B^{\mathrm{out}}$, and $K^{\mathrm{in}} = K^{\mathrm{out}}$, this expression simplifies and reduces to the one in Eq. (11). Furthermore, we considered a droplet of the dense phase in a dilute environment, which is the case for $\bar{\psi} < 0$ (− branch). For $\bar{\psi} > 0$, the interface concentrations swapped resulting in + branch of the solution of Eq. (11).

Furthermore, we can check the scaling of the stationary radius of intensive active droplets in the vicinity of the critical transition. For this, we expand $j_A^{\mathrm{out}}(R) = j_A^{\mathrm{in}}(R)$ for large R. We find the stationary radius R_{stat} as a function of $\bar{\psi}$ that scales like $R_{\mathrm{stat}} \propto |\bar{\psi} - \bar{\psi}_{\mathrm{crit}}|^{-1}$. The general solution can be obtained from the equations above straightforwardly. Because of its length, however, in this appendix we restrict ourselves to the special case of $D_A^{\mathrm{in}} = D_A^{\mathrm{out}} = D_B^{\mathrm{in}} = D_B^{\mathrm{out}} = D$ and $K^{\mathrm{in}} = K^{\mathrm{out}} = K$. We find for the case of a droplet of the dense phase in a dilute environment ($\bar{\psi} < \bar{\psi}_{\mathrm{crit}} < 0$)

$$R_{\mathrm{stat}} = -\Lambda\phi_0 \tan(\beta)\frac{\cos(\alpha)-\sin(\alpha)}{\bar{\psi}-\bar{\psi}_{\mathrm{crit}}}, \tag{E3}$$

where we defined the length scale $\Lambda = \sqrt{D/K}$ and used the fact that, for large droplets, the Laplace pressure becomes negligible.

APPENDIX F: SUPERCRITICAL TRANSITION

Figure 3(c) shows how the stationary droplet radius R_{stat} diverges when the conserved quantity $\bar{\psi}$ approaches the critical value in an infinite system ($R_{\mathrm{syst}} \to \infty$). To investigate the nature of this transition, we calculated the phase fraction $(R_{\mathrm{stat}}/R_{\mathrm{syst}})^3$, i.e., the fraction occupied by the droplet phase, in a finite system for increasing system sizes R_{syst} (see Fig. 9). For intensive droplets, the stable stationary radius R_{stat} is independent of the system size. Thus, the phase volume of the droplet phase $(R_{\mathrm{stat}}/R_{\mathrm{syst}})^3$ approaches zero for large enough system sizes R_{syst}. For extensive droplets, the droplet volume R_{stat}^3 scales with the conserved quantity $\bar{\psi}$ above the critical value of conserved quantity. Above this critical value, there is also an unstable branch. Figure 9 shows that the transition between intensive and extensive droplets gets more pronounced with the phase fraction developing a kink for large system sizes R_{syst}. Thus, the transition is supercritical in the limit of $R_{\mathrm{syst}} \to \infty$.

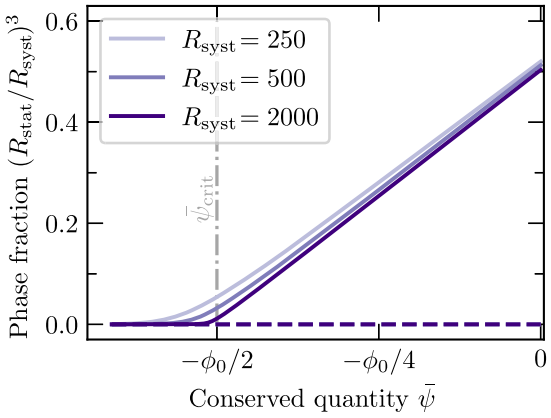

FIG. 9. Critical transition between extensive and intensive droplets. We show the phase fraction $(R_{\mathrm{stat}}/R_{\mathrm{syst}})^3$ of the stable (solid line) and unstable (dashed line) stationary droplet radii as a function of $\bar{\psi}$ for the same parameters as in Fig. 3(c), but in finite systems with system size R_{syst}. For large system sizes, a kink develops and one stable branch transits to two branches (stable and unstable), indicating a supercritical transition.

APPENDIX G: LINEAR STABILITY ANALYSIS

We performed a linear stability analysis around the homogeneous stationary state of the chemical reaction using the free-energy model we introduced in the main text. We consider the chemical reaction scheme in Eqs. (1), which has a unique stationary state for every fixed value of the conserved quantity $\bar{\psi}$. As shown in Fig. 10, depending

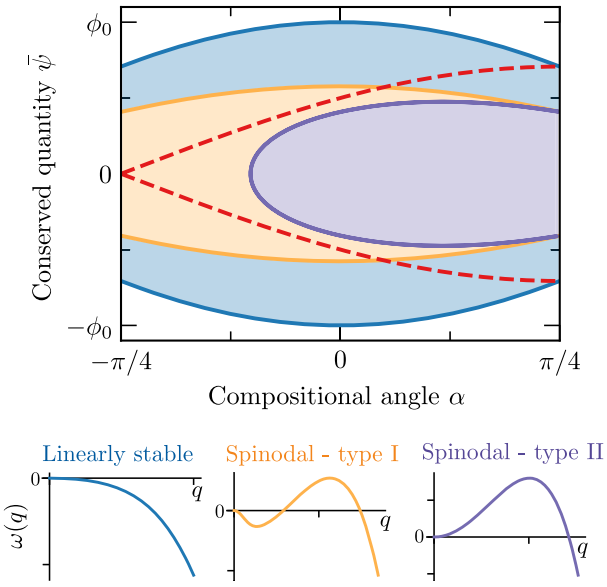

FIG. 10. Linear stability of the homogeneous state. Top: state diagram as shown in Fig. 4 but complemented with the linear stability analysis of the homogeneous state. In the orange domain, a finite range of wave numbers q exists for which $\omega(q) > 0$ (type I instability). In contrast, in the purple domain, there is a type II instability, following the classification of Ref. [66]. Bottom: dispersion relations $\omega(q)$ occurring in the system. In the white and blue domains of the top figure, the homogeneous state is linearly stable, while in the orange (purple) domain, the homogeneous state undergoes a type I (type II) instability. The activity parameter for these figures is $\beta = \pi/4$.

on the compositional angle α, there is a range of conserved quantities $\bar{\psi}$ for which the stationary state lies within the phase-separated domain (colored domains). The boundaries between homogeneous (white domain) and phase-separated (colored domains) stationary states are the binodal lines (blue lines). In the white domain, as expected, any wavelike perturbation $\propto \exp(\omega t - i\boldsymbol{q}\cdot\boldsymbol{x})$ with wave vector $\boldsymbol{q}$ and growth rate $\omega(q)$ decays. Here, $q = |\boldsymbol{q}|$ is the wave number. In a subregion of the phase-separated domain (shaded in blue), sometimes referred to as nucleation and growth, wavelike perturbations also decay. A representative dispersion relation $\omega(q)$ (largest real eigenvalue) of these linearly stable states is shown on the left in the bottom row of Fig. 10, where $\omega(q) < 0$ for all values of q. However, unstable perturbations exist for homogeneous states in the orange and purple domains. In the orange domain, a finite range of q values exists for which $\omega(q) > 0$ (type I instabilities following Ref. [66]), while in the purple domain, even large-scale perturbations with $q \to 0$ become unstable (type II instabilities following Ref. [66]); see the corresponding dispersion relations. Both instabilities lead to the spontaneous demixing of the homogeneous mixture. Note that the classification in terms of type I and type II always refers to the behavior close to instability onset, but not to a change in the dispersion relation that occurs far above the onset, as observed here. In addition, we plot the critical transition line between extensive and intensive droplets (red dashed line in Fig. 10). We conclude that the transition between the two types of dispersion relations (boundary between orange and purple domains) is distinct from the transition between intensive and extensive droplets (red dashed line).

APPENDIX H: PARAMETER CHOICES AND METHODS USED FOR FIGURES

To numerically solve the dynamics equations in this work, we rescale time $t \cdot K$ with K denoting the overall rate [Eq. (10)], and position $\boldsymbol{x}/\ell$ where $\ell = \sqrt{\phi_0^2 \kappa_A / b_1}$, thus, half of the interface width in the continuous model. For simplicity, we consider the overall rate equal inside and outside for all studies ($K^{\text{in}} = K^{\text{out}} = K$). These rescalings yield the following nondimensional parameters in our numerical studies: $D_i^{\text{in/out}}/(\ell^2 K)$, $\gamma c/\ell$, and $\Gamma/(\ell^2 K b_1)$.

1. Figures showing results obtained in the sharp-interface model

In the previous sections, we used the sharp-interface limit to calculate the results shown in Figs. 3(a) and 3(b). Using a standard root-finding scheme, we can numerically solve the specific values of the stationary interfaces shown in Fig. 3 in the main text. The parameter values used to produce these figures are $D_A^{\text{in/out}}/(\ell^2 K) = 0.0014^{-1}$, $D_B^{\text{in/out}}/(\ell^2 K) = 0.0014^{-1}$, $\alpha = 0$, $\beta = 0.12\pi$, $\gamma c/\ell = 1/6$, and $\phi_0 = 1$.

TABLE I. Parameter for grid and system size used for figures showing numerical results obtained from solving the continuous model [Eq. (3)].

	Grid	Size
Fig. 3(b) large	1024×1024	600×600
Fig. 3(b) small	256×256	150×150
Fig. 5	$512 \times 512 \times 128$	$500 \times 500 \times 125$
Fig. 6	$56 \times 256 \times 128$	$250 \times 250 \times 125$
Fig. 7	512×512	550×550
Fig. 8	256×256	150×150
Fig. 8	512×512	300×300
Fig. 8	768×768	450×450
Fig. 8	1024×1024	600×600

2. Figures showing results obtained in the continuous model

All the results obtained in the continuous model were obtained by using an implicit-explicit Runge-Kutta solver of the second-third order. We considered periodic boundary conditions and approximated the higher-order derivatives using pseudospectral methods on a regular lattice. For simplicity, we used $b_1/\phi_0^2 = b_2 = \phi_0 = 1$, $\alpha = 0$, $\kappa_A = \kappa_B$ and $\beta = 0.12\pi$ unless other parameters are explicitly mentioned in the figure caption. The mobilities were set to $\Gamma/(\ell^2 K b_1) = 0.0014^{-1}$ in Fig. 3, $\Gamma/(\ell^2 K b_1) = 0.0028^{-1}$ in Fig. 5, $\Gamma/(\ell^2 K b_1) = 0.00112^{-1}$ in Fig. 6, and $\Gamma/(\ell^2 K b_1 \phi_0^2) = 0.004^{-1}$ in Fig. 7. Furthermore, we used $N_1 \times N_2$ or $N_1 \times N_2 \times N_3$ grid points for two-dimensional or three-dimensional systems of sizes of $L_1 \times L_2$ or $L_1 \times L_2 \times L_3$, respectively. The specific values for the corresponding figures are listed in Table I.

[1] L. A. Williamson and P. B. Blakie, *Universal coarsening dynamics of a quenched ferromagnetic spin-1 condensate*, Phys. Rev. Lett. **116**, 025301 (2016).

[2] Jérôme Bibette, F. Leal Calderon, and P. Poulin, *Emulsions: Basic principles*, Rep. Prog. Phys. **62**, 969 (1999).

[3] Tresa M. Pollock and Ali S. Argon, *Directional coarsening in nickel-base single crystals with high volume fractions of coherent precipitates*, Acta Metall. Mater. **42**, 1859 (1994).

[4] Carl Wagner, *Theorie der alterung von niederschlägen durch umlösen (Ostwald-reifung)*, Z. Elektrochem. Ber. Bunsengesellschaft Phys. Chem. **65**, 581 (1961).

[5] Ilya M. Lifshitz and Vitaly V. Slyozov, *The kinetics of precipitation from supersaturated solid solutions*, J. Phys. Chem. Solids **19**, 35 (1961).

[6] Peter W. Voorhees, *The theory of Ostwald ripening*, J. Stat. Phys. **38**, 231 (1985).

[7] O. Krichevsky and J. Stavans, *Correlated Ostwald ripening in two dimensions*, Phys. Rev. Lett. **70**, 1473 (1993).
[8] M. C. Marchetti, J. F. Joanny, S. Ramaswamy, T. B. Liverpool, J. Prost, Madan Rao, and R. Aditi Simha, *Hydrodynamics of soft active matter*, Rev. Mod. Phys. **85**, 1143 (2013).
[9] Amin Doostmohammadi, Jordi Ignés-Mullol, Julia M. Yeomans, and Francesc Sagués, *Active nematics*, Nat. Commun. **9**, 3246 (2018).
[10] Suraj Shankar, Anton Souslov, Mark J. Bowick, M. Cristina Marchetti, and Vincenzo Vitelli, *Topological active matter*, Nat. Rev. Phys. **4**, 380 (2022).
[11] Christoph A. Weber, David Zwicker, Frank Jülicher, and Chiu Fan Lee, *Physics of active emulsions*, Rep. Prog. Phys. **82**, 064601 (2019).
[12] S. C. Glotzer, D. Stauffer, and N. Jan, *Monte Carlo simulations of phase separation in chemically reactive binary mixtures*, Phys. Rev. Lett. **72**, 4109 (1994).
[13] D. Zwicker, A. A. Hyman, and F. Jülicher, *Suppression of Ostwald ripening in active emulsions*, Phys. Rev. E **92**, 012317 (2015).
[14] Elsen Tjhung, Cesare Nardini, and Michael E. Cates, *Cluster phases and bubbly phase separation in active fluids: Reversal of the Ostwald process*, Phys. Rev. X **8**, 031080 (2018).
[15] F. Brauns, H. Weyer, J. Halatek, J. Yoon, and E. Frey, *Wavelength selection by interrupted coarsening in reaction-diffusion systems*, Phys. Rev. Lett. **126**, 104101 (2021).
[16] H. Weyer, F. Brauns, and E. Frey, *Coarsening and wavelength selection far from equilibrium: A unifying framework based on singular perturbation theory*, Phys. Rev. E **108**, 064202 (2023).
[17] M. E. Cates and C. Nardini, *Active phase separation: New phenomenology from non-equilibrium physics*, Rep. Prog. Phys. **88**, 056601 (2025).
[18] James S. Langer, *Instabilities and pattern formation in crystal growth*, Rev. Mod. Phys. **52**, 1 (1980).
[19] Mark C. Cross and Pierre C. Hohenberg, *Pattern formation outside of equilibrium*, Rev. Mod. Phys. **65**, 851 (1993).
[20] Erwin Frey, Jacob Halatek, Simon Kretschmer, and Petra Schwille, *Protein pattern formation*, *Physics of biological membranes* (Springer, 2018), pp. 229–260, 10.1007/978-3-030-00630-3.
[21] Raphael Wittkowski, Adriano Tiribocchi, Joakim Stenhammar, Rosalind J. Allen, Davide Marenduzzo, and Michael E. Cates, *Scalar φ 4 field theory for active-particle phase separation*, Nat. Commun. **5**, 4351 (2014).
[22] Michael E. Cates, *Active field theories*, *Active Matter and Nonequilibrium Statistical Physics: Lecture Notes of the Les Houches Summer School 2018* (Oxford University Press, 2022), pp. 180–216, https://academic.oup.com/book/45056/chapter-abstract/385614800?redirectedFrom=fulltext&login=false.
[23] Jean David Wurtz and Chiu Fan Lee, *Chemical-reaction-controlled phase separated drops: Formation, size selection, and coarsening*, Phys. Rev. Lett. **120**, 078102 (2018).
[24] Leonardo Demarchi, Andriy Goychuk, Ivan Maryshev, and Erwin Frey, *Enzyme-enriched condensates show self-propulsion, positioning, and coexistence*, Phys. Rev. Lett. **130**, 128401 (2023).
[25] David Zwicker, *Chemically active droplets*, arXiv:2407.09859.
[26] Frank Jülicher and Christoph A. Weber, *Droplet physics and intracellular phase separation*, Annu. Rev. Condens. Matter Phys. **15**, 237 (2024).
[27] Jonas Heckel, Fabio Batti, Robert T. Mathers, and Andreas Walther, *Spinodal decomposition of chemically fueled polymer solutions*, Soft Matter **17**, 5401 (2021).
[28] Patrick S. Schwarz, Sudarshana Laha, Jacqueline Janssen, Tabea Huss, Job Boekhoven, and Christoph A. Weber, *Parasitic behavior in competing chemically fueled reaction cycles*, Chem. Sci. **12**, 7554 (2021).
[29] Karina K. Nakashima, Merlijn HI van Haren, Alain A. M. André, Irina Robu, and Evan Spruijt, *Active coacervate droplets are protocells that grow and resist Ostwald ripening*, Nat. Commun. **12**, 3819 (2021).
[30] Alexander M. Bergmann, Jonathan Bauermann, Giacomo Bartolucci, Carsten Donau, Michele Stasi, Anna-Lena Holtmannspötter, Frank Jülicher, Christoph A. Weber, and Job Boekhoven, *Liquid spherical shells are a non-equilibrium steady state of active droplets*, Nat. Commun. **14**, 6552 (2023).
[31] Jiahua Wang, Manzar Abbas, Junyou Wang, and Evan Spruijt, *Selective amide bond formation in redox-active coacervate protocells*, Nat. Commun. **14**, 8492 (2023).
[32] Judit Sastre, Advait Thatte, Alexander M. Bergmann, Michele Stasi, Marta Tena-Solsona, Christoph A. Weber, and Job Boekhoven, *Size control and oscillations of active droplets in synthetic cells*, Nat. Commun. **16**, 2003 (2025).
[33] Clifford P. Brangwynne, Christian R. Eckmann, David S. Courson, Agata Rybarska, Carsten Hoege, Jöbin Gharakhani, Frank Jülicher, and Anthony A. Hyman, *Germline P granules are liquid droplets that localize by controlled dissolution/condensation*, Science **324**, 1729 (2009).
[34] Marina Feric, Nilesh Vaidya, Tyler S. Harmon, Diana M. Mitrea, Lian Zhu, Tiffany M. Richardson, Richard W. Kriwacki, Rohit V. Pappu, and Clifford P. Brangwynne, *Coexisting liquid phases underlie nucleolar subcompartments*, Cell **165**, 1686 (2016).
[35] Yongdae Shin and Clifford P. Brangwynne, *Liquid phase condensation in cell physiology and disease*, Science **357**, eaaf4382 (2017).
[36] Steven Boeynaems, Simon Alberti, Nicolas L. Fawzi, Tanja Mittag, Magdalini Polymenidou, Frederic Rousseau, Joost Schymkowitz, James Shorter, Benjamin Wolozin, Ludo Van Den Bosch, Peter Tompa, and Monika Fuxreiter, *Protein phase separation: A new phase in cell biology*, Trends Cell Biol. **28**, 420 (2018).
[37] P. C. Matthews and S. M. Cox, *Pattern formation with a conservation law*, Nonlinearity **13**, 1293 (2000).
[38] Tohru Okuzono and Takao Ohta, *Traveling waves in phase-separating reactive mixtures*, Phys. Rev. E **67** (2003).
[39] Mikiya Otsuji, Shuji Ishihara, Carl Co, Kozo Kaibuchi, Atsushi Mochizuki, and Shinya Kuroda, *A mass conserved reaction–diffusion system captures properties of cell polarity*, PLoS Comput. Biol. **3**, e108 (2007).
[40] Shuji Ishihara, Mikiya Otsuji, and Atsushi Mochizuki, *Transient and steady state of mass-conserved reaction-diffusion systems*, Phys. Rev. E **75** (2007).
[41] Jacob Halatek and Erwin Frey, *Rethinking pattern formation in reaction-diffusion systems*, Nat. Phys. **14**, 507 (2018).

[42] Tom Burkart, Manon C. Wigbers, Laeschkir Würthner, and Erwin Frey, *Control of protein-based pattern formation via guiding cues*, Nat. Rev. Phys. **4**, 511 (2022).

[43] David Zwicker, Rabea Seyboldt, Christoph A. Weber, Anthony A. Hyman, and Frank Jülicher, *Growth and division of active droplets provides a model for protocells*, Nat. Phys. **13**, 408 (2017).

[44] Rabea Seyboldt and Frank Jülicher, *Role of hydrodynamic flows in chemically driven droplet division*, New J. Phys. **20**, 105010 (2018).

[45] Jonathan Bauermann, Christoph A. Weber, and Frank Jülicher, *Energy and matter supply for active droplets*, Ann. Phys. (Berlin) **534**, 2200132 (2022).

[46] Giacomo Bartolucci, Omar Adame-Arana, Xueping Zhao, and Christoph A. Weber, *Controlling composition of coexisting phases via molecular transitions*, Biophys. J. **120**, 4682 (2021).

[47] J. Bauermann, G. Bartolucci, J. Boekhoven, C. A. Weber, and F. Jülicher, *Formation of liquid shells in active droplet systems*, Phys. Rev. Res. **5**, 043246 (2023).

[48] Chaohui Tong and Yuliang Yang, *Phase-separation dynamics of a ternary mixture coupled with reversible chemical reaction*, J. Chem. Phys. **116**, 1519 (2002).

[49] Jan Kirschbaum and David Zwicker, *Controlling biomolecular condensates via chemical reactions*, J. R. Soc. Interface **18**, 20210255 (2021).

[50] P. C. Hohenberg and B. I. Halperin, *Theory of dynamic critical phenomena*, Rev. Mod. Phys. **49**, 435 (1977).

[51] Jonathan Bauermann, Sudarshana Laha, Patrick M. McCall, Frank Jülicher, and Christoph A. Weber, *Chemical kinetics and mass action in coexisting phases*, J. Am. Chem. Soc. **144**, 19294 (2022).

[52] R. Lefever, D. Carati, and N. Hassani, *Comment on "Monte Carlo simulations of phase separation in chemically reactive binary mixtures"*, Phys. Rev. Lett. **75**, 1674 (1995).

[53] Sharon C. Glotzer, Dietrich Stauffer, and Naeem Jan, *Glotzer, Stauffer, and Jan reply*, Phys. Rev. Lett. **75**, 1675 (1995).

[54] Samuel Safran, *Statistical Thermodynamics of Surfaces, Interfaces, and Membranes* (CRC Press, Boca Raton, FL, 2019).

[55] Mehran Kardar, *Statistical Physics of Fields* (Cambridge University Press, Cambridge, England, 2007).

[56] Dan Deviri and Samuel A. Safran, *Physical theory of biological noise buffering by multicomponent phase separation*, Proc. Natl. Acad. Sci. U.S.A. **118**, e2100099118 (2021).

[57] Xiangze Zeng and Rohit V. Pappu, *Developments in describing equilibrium phase transitions of multivalent associative macromolecules*, Curr. Opin. Struct. Biol. **79**, 102540 (2023).

[58] F. C. Thewes, M. Krüger, and P. Sollich, *Composition dependent instabilities in mixtures with many components*, Phys. Rev. Lett. **131**, 058401 (2023).

[59] Joshua A. Riback, Lian Zhu, Mylene C. Ferrolino, Michele Tolbert, Diana M. Mitrea, David W. Sanders, Ming-Tzo Wei, Richard W. Kriwacki, and Clifford P. Brangwynne, *Composition-dependent thermodynamics of intracellular phase separation*, Nature (London) **581**, 209 (2020).

[60] Sudarshana Laha, Jonathan Bauermann, Frank Jülicher, Thomas C. T. Michaels, and Christoph A. Weber, *Chemical reactions regulated by phase-separated condensates*, Phys. Rev. Res. **6** (2024).

[61] M. Bestehorn and D. Merkt, *Regular surface patterns on Rayleigh-Taylor unstable evaporating films heated from below*, Phys. Rev. Lett. **97**, 127802 (2006).

[62] U. Oono and Y. Shiwa, *Computationally efficient modeling of block copolymer and Benard pattern formations*, Mod. Phys. Lett. B **01**, 49 (1987).

[63] Y. Oono and S. Puri, *Study of phase-separation dynamics by use of cell dynamical systems. I. Modeling*, Phys. Rev. A **38**, 434 (1988).

[64] Pierluigi Colli, Gianni Gilardi, Elisabetta Rocca, and Jürgen Sprekels, *Well-posedness and optimal control for a Cahn-Hilliard-Oono system with control in the mass term*, arXiv:2108.03165.

[65] A. J. Bray, *Theory of phase-ordering kinetics*, Adv. Phys. **43**, 357 (1994).

[66] Michael Cross and Henry Greenside, *Pattern Formation and Dynamics in Nonequilibrium Systems* (Cambridge University Press, Cambridge, England, 2009).

[67] Jonathan Bauermann, Giacomo Bartolucci, Christoph A. Weber, and Frank Jülicher, *The droplet size distribution and its dynamics in chemically active emulsions*, Phys. Rev. Lett. **135**, 148201 (2025).

[68] See Supplemental Material at http://link.aps.org/supplemental/10.1103/4nnd-tdky for a movies of the corresponding ripening dynamics.

[69] M. E. Cates and C. Nardini, *Classical nucleation theory for active fluid phase separation*, Phys. Rev. Lett. **130**, 098203 (2023).

[70] N. Ziethen, J. Kirschbaum, and D. Zwicker, *Nucleation of chemically active droplets*, Phys. Rev. Lett. **130**, 248201 (2023).

[71] Carsten Donau, Fabian Späth, Marilyne Sosson, Brigitte A. K. Kriebisch, Fabian Schnitter, Marta Tena-Solsona, Hyun-Seo Kang, Elia Salibi, Michael Sattler, Hannes Mutschler, and Job Boekhoven, *Active coacervate droplets as a model for membraneless organelles and protocells*, Nat. Commun. **11**, 5167 (2020).

[72] Elsen Tjhung, Cesare Nardini, and Michael E. Cates, *Cluster phases and bubbly phase separation in active fluids: Reversal of the Ostwald process*, Phys. Rev. X **8**, 031080 (2018).

[73] Fabian Bergmann, Lisa Rapp, and Walter Zimmermann, *Active phase separation: A universal approach*, Phys. Rev. E **98** (2018).

[74] Suropriya Saha, Jaime Agudo-Canalejo, and Ramin Golestanian, *Scalar active mixtures: The nonreciprocal Cahn-Hilliard model*, Phys. Rev. X **10**, 041009 (2020).

[75] T. Frohoff-Hülsmann and U. Thiele, *Nonreciprocal Cahn-Hilliard model emerges as a universal amplitude equation*, Phys. Rev. Lett. **131**, 107201 (2023).

[76] T. Suchanek, K. Kroy, and S. A. M. Loos, *Entropy production in the nonreciprocal Cahn-Hilliard model*, Phys. Rev. E **108**, 064610 (2023).

[77] F. Brauns and M. C. Marchetti, *Nonreciprocal pattern formation of conserved fields*, Phys. Rev. X **14**, 021014 (2024).